# Measurements of Turbulence in the Upper-Ocean Mixing Layer Using Autosub

S. A. THORPE

*Southampton Oceanography Centre, Southampton, United Kingdom*

T. R. OSBORN

*Department of Earth and Planetary Science, The Johns Hopkins University, Baltimore, Maryland*

J. F. E. JACKSON AND A. J. HALL

*Southampton Oceanography Centre, Southampton, United Kingdom*

R. G. LUECK

*Ocean Turbulence Laboratory, University of Victoria, Victoria, British Columbia, Canada*

(Manuscript received 25 October 2001, in final form 12 June 2002)

ABSTRACT

The rate of dissipation of turbulent kinetic energy has been measured with airfoil probes mounted on an autonomous vehicle, Autosub, on constant-depth legs at 2–10 m below the surface in winds up to 14 m $s^{-1}$. The observations are mostly in an area limited by fetch to 26 km where the pycnocline depth is about 20 m. At the operational depths of 1.55–15.9 times the significant wave height $H_s$, and in steady winds of about 11.6 m $s^{-1}$ when the wave age is 11.7–17.2, dissipation is found to be lognormally distributed with a law-of-the-wall variation with depth and friction velocity. Breaking waves, leaving clouds of bubbles in the water, are detected ahead of the Autosub by a forward-pointing sidescan sonar, and the dissipation is measured when the clouds are subsequently reached. Bands of bubbles resulting from the presence of Langmuir circulation are identified by a semiobjective method that seeks continuity of band structure recognized by both forward- and sideways-pointing sidescan sonars. The times at which bands are crossed are determined and are used to relate dissipation rates and other measured parameters to the location of Langmuir bands. Shear-induced ‘‘temperature ramps’’ are identified with large horizontal temperature gradients. The turbulence measurements are consequently related to breaking waves, the bubble clouds, Langmuir circulation, and temperature ramps, and therefore to the principal processes of mixing in the near-surface layer of the ocean, all of which are found to have associated patterns of turbulent dissipation rates. A large proportion of the highest values of dissipation rate occur within bubble clouds. Dissipation is enhanced in the convergence region of Langmuir circulation at depths to about 10 m, and on the colder, bubble containing, side of temperature ramps associated with water advected downward from near the surface. Near the sea surface, turbulence is dominated by the breaking waves; below a depth of about $6H_s$ the local vertical mixing in stronger Langmuir circulation cells exceeds that produced on average by the shear-induced eddies that form temperature ramps.

## 1. Introduction

Momentum and gas exchange between the atmosphere and the ocean are known to involve wave breaking, bubble and turbulence generation, mixing by Langmuir circulation (hereinafter, for brevity, referred to as Lc) and shear-induced turbulence, all of them processes that are poorly known. This is an investigation of the relative contributions of these processes to turbulence in the upper ocean.

*Corresponding author address:* Dr. S. A. Thorpe, ‘‘Bodfryn,’’ Glanrafon, Llangoed, Anglesey LL58 8PH, United Kingdom.
E-mail: sxt@soc.soton.ac.uk



In January 1988 efforts to make measurements of turbulence and bubbles from the U.S. Navy Research Submarine *Dolphin* were largely frustrated by a major failure in the submarine's generators at an early stage of the experiment (Osborn et al. 1992). While the results were consequently fragmentary and rather inconclusive, turbulent dissipation rates were found to be enhanced within acoustically detected bubble clouds and turbulent dissipation was observed to exceed that predicted by law of the wall scaling,

$$\epsilon = u_{*w}^3/kz, \qquad (1)$$

in the upper 2–4 m in winds of 5–9 m $s^{-1}$. In (1) $\epsilon$ is the rate of dissipation of turbulent kinetic energy per unit mass, $k$ is von Kármán's constant (about 0.41), and $u_{*w}$ is the friction velocity in the water. [An approximate relation between the friction velocities in the water and the air is provided by Mitsuyasu (1985) who notes that, since the momentum flux divergence in the wave field is small, most of the momentum transferred from the wind to the wave field is passed on directly into the water so that the wind stress on the water surface, $\tau$, is approximately equal to that in the water, i.e. $\tau = \rho_a u_*^2$, $= \rho_w u_{*w}^2$, where and $\rho_a$, $\rho_w$ are the air and water densities, respectively. Therefore, since $\rho_a/\rho_w$ is about $1.2 \times 10^{-3}$, $u_{*w} \approx 0.035 u_*$. In the following we shall assume that $\tau$ is given by $\tau = C_D \rho_a W_{10}^2$, where $W_{10}$ is the wind speed (m s$^{-1}$) at 10-m height and $C_D$ is the drag coefficient given by Geernaert (1990) as $C_D = 10^{-3} \times (0.75 + 0.067 W_{10})$.]

Some of the objectives not achieved in the *Dolphin* experiment have been addressed using an automated underwater vehicle (AUV), Autosub (Millard et al. 1998), as a platform to carry the turbulence and other sensors. Simultaneous measurements of turbulent dissipation and acoustic scattering from subsurface bubbles at depths between 2 and 10 m in wind speeds ranging from calm to 14 m s$^{-1}$ were made in March–April 2000. The vehicle, the sensors used, and the analysis of the measurements are described below.

Since the time of the experiment in 1988, knowledge of breaking waves, near-surface turbulence, bubble clouds, and Lc has increased, largely as a consequence of novel means of observation. There is also an increased awareness of the importance of these connected processes in the air–sea exchange of momentum and gases, which are factors affecting climate change [e.g., see Farmer et al. (1993) and reviews by Thorpe (1995) and Melville (1996)].

The way in which turbulence generated by a breaking wave penetrates the water column and decays is described from the laboratory experiments by Rapp and Melville (1990), although these are in the *absence* of preexisting subsurface turbulence, Lc and shear, and so possibly give only approximate estimates of the evolution of turbulence and flow that might be found in the open ocean. The maximum depth of turbulence grows rapidly and extends downward, reaching depths of $(0.75 \pm 0.1)H$ for spilling breakers and $(1.35 \pm 0.35)H$ for plunging breakers at a time of one wave period after breaking, where $H$ is the height of the breaking wave. Thereafter the rate of spread decreases, with turbulence reaching $(1.7 \pm 0.3)H$ for spilling breakers and $(2.5 \pm 0.5)H$ at 13 wave periods after generation, with turbulent energy decaying at a rate proportional to $t^{-1}$, but with velocity fluctuations of magnitude $0.005 c_b$ remaining after 60 wave periods, where $c_b$ is the phase speed of the breaking wave. More than 90% of the energy lost by the waves is dissipated within 4 wave periods after breaking. Dye released at the breaker location in the laboratory studies acts as an indicator of the turbulent region and is spread horizontally to a length of about one wavelength about the breaker location. A weak residual rotor circulation can be detected for some 50 wave periods after breaking. Lamarre and Melville (1991) find that 30% to 50% of the energy lost by breakers may be expended in the formation of bubbles.

Duncan (1981) made laboratory experiments in which a steady breaking wave is produced by a towed hydrofoil. Measurements of the drag on the hydrofoil are used to infer a dissipation rate per unit crest length of the breaker of $\chi \rho_w c_b^5/g$, where $\chi$ depends on the spilling or plunging nature of the breaking wave. Taking into account the range of breaker types and the unsteady nature of breaking waves at sea and using the earlier results of Rapp and Melville, Melville (1994) suggests that $\chi = 0.008 \pm 0.004$.

The paper by Agarwal et al. (1992) had a significant impact on the development of ideas about near-surface turbulence and the effect of breaking waves; turbulent dissipation rates exceed those of (1) to depths, $z$, of about $10^5 u_{*w}^2/g$, where $g$ is the acceleration due to gravity. Terray et al. (1996) suggest that the significant wave height $H_s$ and the wave age $c/u_*$ are important in scaling dissipation, where $c$ is the phase speed of waves at the peak of the wave frequency spectrum. They find a near-surface region extending to a depth, $z_b = 0.6 H_s$, which is strongly affected by breaking waves, in which $\epsilon$ is nearly constant, and where about half the net loss of energy by the breaking waves is dissipated. Below this is a layer where $\epsilon$ still exceeds the value (1), and is given by

$$\epsilon = 0.3 H_s c' u_{*w}^2 / z^2, \tag{2}$$

for ‘‘young’’ waves with $4.3 < c/u_* < 7.4$. This layer extends from $z_b$ to a depth $z_t = (3.6 c'/u_*) H_s$, where $c'$ is a speed related to the rate of energy input from the wind, $F$, through the relation $F = \tau c'$. Terray et al. present data that, although scattered, suggests that $c'/c \approx (10 u_*/c - 0.25)$ when the wave age $c/u_* > 13.3$ and $c'/c \approx 0.5$ when $4 < c/u_* < 13.3$. In the latter range, $z_t$ is approximately equal to $1.8 H_s c/u_*$. Equation (2) is consistent with data collected by Drennan et al. (1996), although there is considerable scatter and uncertainty in the depth relationship. At depths $z > z_t$, dissipation appears to follow the relation (1).

Terray et al.'s results are still controversial. Indeed Anis and Moum (1995) find a $z^{-3}$ dissipation decay law based on their analysis of microstructure probe measurements, and Craig and Banner (1994) derive $z^{-3.4}$ decay on the basis of a second-order turbulent closure model. In their analysis of near-surface temperature microstructure, Gemmrich and Farmer (1999a) find a near-surface turbulent diffusion scale of about 0.2 m, much less than the scale, $H_s$ (about 3 m in their observations), which is suggested by Terray et al. Gemmrich and Farmer remark that the discrepancy is ‘‘puzzling’’ and call for further observations. The waves that contribute most to breaking at sea have periods between 10% and 130% of that of the dominant waves, with a mean of 54% and with 77% of measured values lying between 20% and 80% (Gemmrich and Farmer 1999b), a range which implies a similar spread in phase speeds. Duncan's (1981) finding that the energy lost per unit crest length from a breaker depends on the fifth power of its phase speed, together with Gemmrich and Farmer's results, implies a very broad variation in the energy lost from the waves and in the subsequent dissipation. Gemmrich and Farmer (1999b) conclude that the breaking wave height is typically only some $0.7H_s$ (but with much scatter). They also find that the period between breakers is better represented by a parameter proportional to the ratio of the rate of transfer of wind energy into the wave field divided by that of the transfer at the same wind speed into a fully developed wave field than by wave age. This suggests that a scaling of near-surface turbulence with $H_s$, $c'$, $u_{*w}$, and $z$ alone may be too simplistic.

As yet, the processes of bubble generation and injection into the upper ocean are poorly known. A rapid downward spread of bubbles from breaking waves has however been observed by Farmer et al. (1999) in winds of about 12 m $s^{-1}$. Their measurements show that a rise in air (or void) fraction from the background levels of about $5 \times 10^{-8}$ to about $10^{-5}$ occurs within about 4 s after wave breaking at depths less than about 1.3-m, with smaller increase at 1.9 m and scarcely any at 3.3 m. The air fraction decreases over a subsequent period of about 60 s, consistent with earlier observations of bubble cloud decay following wave breaking (Thorpe and Hall 1983). On average bubble clouds are elongated downwind with aspect ratio of downwind length to across-wind width about 1.5. The ratio of the downwind extent to wavelength increases from about 0.1 to 1.2 as $W_{10}/c$ increases from 0.8 to 1.7 (Thorpe 1986b).

Several different kinds of large-scale coherent structures are known to exist within the upper ocean boundary layer. Often the most evident is Lc. The generation of Lc is generally accepted as being a consequence of Craik–Leibovich instability of perturbations to the near-surface flow field in the presence of wind shear and Stokes drift in the wind wave field, a downwind component of vorticity growing as a result of the vortex force (Leibovich 1983). This mechanism has provided the basis of numerical large eddy simulation models, which replicate many of the properties of Lc observed in the ocean (Skyllingstad and Danbo 1995; McWilliams et al. 1997). Windrows form at the surface in the zones of surface convergence between neighboring pairs of downwind-aligned vortices of alternating sign (the Langmuir ''cells''). Below these windrows the flow is downward with speeds reaching 0.2 m $s^{-1}$ (Weller and Price 1988), but usually less. The circulation advects subsurface bubbles that accumulate in the downward-going flow and form bubble bands detectable using sidescan sonar (Thorpe 1984; Zedel and Farmer 1991). The windrows and bubble bands have an hierarchy of cell scales, the largest persisting longest. The mean depth of bubble clouds based on the analysis of 250-kHz acoustic data obtained far from shore is about $4H_s$ and the maximum plume depth is of order $6H_s$ (Thorpe 1995). Although the supply of bubbles is provided by breaking waves, these penetration depths appear to be determined by downward advection in the Langmuir convergence zones, bubble rise and dissolution, rather than by the turbulence in breaking waves (Zedel and Farmer 1991). Furthermore, waves do not appear to break more frequently in windrows (Thorpe 1992b).

Once regarded as being a quasi-steady phenomenon, the vortical motions described as Lc are now known to be unsteady and turbulent, more so in deep water and in high winds than in shallow water or low winds (Thorpe 1992a; Leibovich and Tandon 1993; Li and Garrett 1993; Farmer and Li 1995). The instability of Lc is characterized by the amalgamation of neighboring cells. Some of the observed transience and broadband structure of the windrow patterns may be a consequence of the direct injection of a vertical component of vorticity around the edges of breaking waves (a finite-amplitude perturbation to the mean flow) and its subsequent distortion by the Stokes drift, resulting in pairs of mutually interacting vortices with horizontal axes which first converge, interacting most strongly with their images in the water surface and then propagate downward away from the sea surface (Csanady 1994).

The advection of bubble clouds and associated decaying turbulence produced by breaking waves toward regions of convergence makes it likely that some turbulence enhancement occurs near these regions, although no previous observations have been made to confirm this. A vertical decay of the strength of the Lc over a scale $(2k)^{-1}$, similar to that of the Stokes drift that is instrumental in its forcing (Leibovich 1983), is consistent with observations of vertical circulation by Weller and Price (1988) and suggests a vertical scale for such enhanced dissipation.

One effect of Lc is the production of temperature anomalies of a few millikevin beneath the windrows. These are detected to depths of several meters and indicate the downward advective transfer of near-surface water that is warmed or cooled through air–sea heat transfer (e.g., see Thorpe and Hall 1982). The linear bands of temperature anomalies detected by infrared imagery of the ocean surface by McLeish (1970) presumably result from spatial variations in the structure of the conductive ''surface skin'' in response to the convergent flow into windrows, the accumulation of surfactants there, and the variation of the underlying water temperature. Gemmrich and Farmer (1999a) report temperature anomalies produced by breakers in a sea with $H_s \approx 3$–5 m and winds of 15 m $s^{-1}$. These anomalies are, however, rarely detectable at depth 0.26 m following wave breaking and only last for about 1 s. Gemmrich (2000) proposes a model, based on his observations with Farmer (Farmer and Gemmrich 1996; Gemmrich and Farmer 1999a,b), in which there is a patchy, but typically 3–5 cm thick, near-surface layer of anomalous temperature that is periodically subducted by breaking waves in a wave field with $H_s = 2$–5 m. The cold skin of the ocean is found to contain too little heat to be important in supporting the observed temperature changes associated with wave breaking. The temperature of the layer 3–5 cm is determined by the surface heat flux (including downwelling solar radiation to the depth of the layer). How the near-surface layer is maintained is not clear, but turbulence and turbulent bursts generated by microbreakers (e.g., Jessup et al. 1997) appear to offer one possibility. Upwelling and the stripping off of this surface thermal layer by Lc, and turbulence from larger breaking waves, may contribute to its patchy structure and may be the source of the temperature anomalies beneath windrows. It appears that Lc is responsible for much of the vertical transport of heat below a depth that may be a small fraction of $H_s$, and that direct injection of heat to significant depths by breakers is relatively unimportant. How Lc affects the vertical distribution of turbulent dissipation is considered later (see sections 3d and 4c).

The second coherent structure of the upper ocean boundary layer is manifested by the presence of ''temperature ramps'' or ''microfronts,'' spatially narrow tilted surfaces across which there is a temperature change, usually of a few millikevin. These appear to be caused by the straining of the ambient temperature field in eddies with axes orientated mainly parallel to the vorticity vector of the mean shear. Such coherent eddies are a common feature of turbulent shear flows (Brown and Roshko 1974). Temperature ramps are also known to occur in the atmospheric boundary layer (Antonia et al. 1979) and in laboratory studies of turbulent stratified shear flow (e.g., see Keller and Van Atta 2000). In lakes and in the upper ocean, these structures may indicate that the mean flow with its accompanying stratification is near marginal stability (Thorpe and Hall 1977; Thorpe 1978). Numerical studies by Gerz et al. (1994) and Gerz and Schumann (1996) offer an explanation in terms of hairpin or horseshoe vortex structures. Whatever the explanation, as a consequence of the presence of the enhanced temperature gradients, the skewness, $S$, of the temperature time derivative measured from a platform moving much faster than the mean flow varies roughly sinusoidally with direction relative to the wind. Opposite signs of $S$ (typically of order $\pm 1$) are observed when tows of recording temperature sensors are made along reverse tracks up and down wind, with values close to zero for across-wind tracks (Thorpe 1985). For steady and persistent winds, there is some evidence of the effect of the earth's rotation, and the ramp structure is turned to be transverse to the flow associated with the near-surface Ekman spiral (Thorpe et al. 1991) leading to small, nonzero, across-wind values of $S$. Skewness values measured on upwind tracks are positive when there is a positive flux of heat into the water through the surface and negative in convectively unstable conditions of heating, that is, surface heat loss. There is evidence that the eddies causing ramps can entrain and vertically advect bubbles (Thorpe and Hall 1987), that velocity changes occur across temperature ramps (Thorpe and Hall 1980), and that close to the surface they are sometimes related to the occurence of breaking waves (Thorpe and Hall 1987; Farmer and Gemmrich 1996). How the coherent structures associated with temperature ramps are related to and affect the distribution of turbulent dissipation is described below (see sections 3e and 4d).

A third coherent structure is that associated with penetrative convection. This is expected to occur in conditions of surface cooling or buoyancy loss and at depths beyond the region of mechanical mixing from the surface, depths beyond about twice the modulus of the Monin–Obukov length scale. In view of the similarity in scaling of dissipation (Shay and Gregg 1986), the structure of convective features should resemble that of the plumes or banded structures observed in a convective atmospheric boundary layer. The present observations made relatively close to the surface in near-neutral heating conditions do not add to their understanding. ''Rollers'' formed by breaking waves are a further coherent structure within the upper ocean, but in laboratory studies extend only to a depth of about $H_s$, above the depth range of the present observations (Melville et al. 2002).

Section 2 describes the dataset and methodology used in analysis that is nonstandard. Some of this might be skipped by the reader who wishes only to see the description of the main observations in section 3 and their discussion in section 4. The objective is to describe how the rate of dissipation of turbulent kinetic energy is affected by breaking waves and associated bubble clouds, and by Lc and temperature ramps. Sections 2–4 are divided into subsections accordingly.

## 2. Data and analysis methods

### a. The dataset

Four ''missions'' were run off the coast of northwest Scotland between the islands of Mull and Colonsey and to the west of Colonsay in water depths ranging from 40 to 110 m using an AUV, Autosub (Millard et al. 1998). Autosub carried CTD, ADCP, a turbulence dissipation package, and forward- and starboard-pointing sidescan sonars (see the appendix). Its speed through the water was about 1.25 m s$^{-1}$. The missions each involved deployment and recovery of the vehicle, return to shelter (at Dunstaffnage, near Oban), and subsequent ''stripping off'' of recorded data, the latter taking some 5–6 hours. A total of 112 h of data were recorded mainly with Autosub running ''legs'' at constant nominal depths of 2 m (or occasionally 3 m when swell was appreciable), 4 m, 6 m, and 10 m, along 5-km sides of a square, each taking about 1 h. Actual mean depths and environmental data on legs are given in Table 1.

TABLE 1. Environmental data. The table columns, left to right, list mission/leg numbers, Autosub depth ($z$), the standard deviation of $z$, the course direction, wind speed ($W_{10}$), wind direction ($\theta$), the significant wave height of the wind waves ($H_s$), the wind wave period ($T_w$) and swell (calculated as explained in section 3c), and the skewness of the temperature derivative [$S(dT/dt)$].

| Mission Leg | Depth (m) | | Course (°) | Wind speed (m s$^{-1}$) | Wind direction (°) | $H_s$ (m) | Wave period (s) | Swell | | $S(dT/dt)$ |
|---|---|---|---|---|---|---|---|---|---|---|
| | Actual | Std dev | | | | | | | | |
| 1.1 | 2.23 | 0.42 | 61 | 12.4 | 112 | 1.08 | | | | −0.37 |
| 1.2 | 2.21 | 0.34 | 331 | 10.6 | 90 | 0.93 | | | | −0.51 |
| 1.3 | 4.10 | 0.22 | 241 | 11.4 | 90 | 0.92 | | | | 0.70 |
| 1.4 | 4.02 | 0.18 | 151 | 11.9 | 100 | 0.95 | | | | −0.50 |
| 1.5 | 6.11 | 0.16 | 61 | 11.0 | 110 | 1.26 | | | | −0.96 |
| 1.6 | 6.09 | 0.19 | 331 | 11.5 | 110 | 0.87 | | Slight ~0.1 m | | 0.54 |
| 1.7 | 10.44 | 0.12 | 241 | 12.9 | 110 | 0.94 | 3.9-4.0 | | | 0.14 |
| 1.8 | 10.43 | 0.11 | 151 | 11.7 | 110 | 1.05 | | Period 9–11s | | −1.17 |
| 1.9 | 3.99 | 0.18 | 61 | 11.6 | | 1.15 | | | | −0.92 |
| 1.10 | 4.06 | 0.23 | 331 | 12.1 | 100 | 0.87 | | | | 1.26 |
| 1.13 | 10.42 | 0.12 | 61 | 12.1 | 110 | 0.76 | | | | −0.37 |
| 1.14 | 10.43 | 0.11 | 331 | 10.2 | 110 | 0.66 | | | | 0.52 |
| 1.15 | 1.92 | 0.27 | 241 | 9.5 | 110 | 0.81 | | | | 0.04 |
| 1.16 | 2.04 | 0.33 | 151 | 10.8 | | 0.94 | | | | −1.08 |
| 1.17 | 10.39 | 0.11 | 120 | 9.1 | 110–145 | 0.94 | | | | −1.13 |
| 2.1 | 2.14 | 0.33 | 60 | 8.2 | 190 ± 10 | 0.82 | 3.2 | Swell period | 1.60 | 0.30 |
| 2.2 | 2.10 | 0.27 | 331 | 8.2 | 190 ± 10 | 0.82 | 3.2 | ~10 s from SW | 1.60 | 0.61 |
| 2.12 | 2.95 | 0.13 | 60 | 5.5 | 44 | 0.93 | 2.5 | | 1.15 | −1.05 |
| 2.13 | 2.87 | 0.07 | 330 | 5.5 | 42 | 0.43 | 3.2 | Period 6–8 s | 0.77 | −0.24 |
| 2.14 | 3.94 | 0.07 | 240 | 4.8 | 14 | 0.40 | 3.1 | From SW | 0.70 | 0.68 |
| 2.15 | 3.93 | 0.04 | 150 | 4.0 | 357 | 0.22 | 2.8 | | 0.76 | −0.66 |
| 3.1 | 1.70 | 0.26 | 241 | 6.0 | 65 | 0.46 | 3.2 | From SW | 0.43 | 0.51 |
| 3.2 | 1.57 | 0.11 | 149 | 5.5 | 45 | 0.41 | 3.1 | | 0.55 | 1.02 |
| 3.3 | 3.64 | 0.09 | 61 | 5.0 | 129 | 0.69 | 2.9 | | 0.48 | −0.35 |
| 3.4 | 3.59 | 0.04 | 331 | 4.3 | 110 | 0.14 | 2.9 | | 0.36 | 0.80 |
| 3.5 | 5.77 | 0.05 | 241 | 3.6 | 104 | 0.14 | 2.8 | | 0.39 | 1.37 |
| 3.6 | 5.76 | 0.04 | 149 | 3.0 | 105 | 0.14 | 2.6 | | 0.37 | −1.09 |
| 4.22 | 1.60 | 0.25 | 151 | 12.0 | 55 | 1.01 | 4.6 | | | −2.25 |
| 4.23 | 1.72 | 0.35 | 61 | 12.0 | 51 | 1.11 | 4.3 | Slight ~0.1 m | | −0.65 |
| 4.24 | 5.76 | 0.12 | 330 | 12.0 | 41 | 1.06 | 4.8 | | | −0.10 |
| 4.25 | 5.83 | 0.16 | 239 | 12.0 | 50 | 0.81 | 5.2 | Period 10–11 s | | 0.97 |
| 4.26 | 3.57 | 0.12 | 151 | 13.0 | 50 | 0.85 | 4.4 | | | −0.01 |
| 4.27 | 3.64 | 0.19 | 61 | 11.0 | 48 | 1.17 | 3.8 | | | −0.70 |
| 4.28 | 10.10 | 0.09 | 330 | 11.5 | 35 | 0.79 | 4.3 | | | −0.14 |

Winds recorded aboard the mother vessel, the *Terschelling*, used for deployment and recovery, were mainly offshore, limiting the fetch to between 8 and 26 km. In consequence, waves were fetch limited, with probably more frequent plunging breakers and relatively deep bubble cloud penetration than in comparable open-sea conditions (e.g., see Gemmrich and Farmer 1999b). Most of the data described below are obtained in relatively steady winds with average wind speed of 11.6 m s$^{-1}$ (mission 1, legs 1–16, and mission 4, legs 22–28). The lower winds averaging 4.7 m s$^{-1}$ (mission 2, legs 12–16, and mission 3, legs 1–6) are unsteady and swell is present making interpretation of the data consequently more difficult and uncertain. In relatively steady winds in mission 1 with a mean fetch of about 21 km, the average $W_{10}$ is 11.4 m s$^{-1}$ with corresponding $u_* = 0.44$ m s$^{-1}$. Wave height is $H_s = 0.94$ m with dominant windwave period, $T_w = 3.9$ s, giving $c = 6.1$ m s$^{-1}$ from the dispersion relation and a wave age of 14. The values of fetch, $X$, and $H_s$ can be compared with $X = 19.0$ km and $H_s = 0.97$ m calculated from the general formulas $gX/u_*^2 = 358(c/u_*)^3$ and $gH_s/u_*^2 = 0.96(c/u_*)^{3/2}$ given by Csanady (2001).

Dives were made on the completion of each square to check the vertical $T$–$S$ structure of the water column. The mixed layer depth was at least 12 m (usually about 20 m), greater than the maximum depth of the legs run by Autosub. Below the mixed layer the temperature and salinity both rose, temperature by 0.2–0.3 K and salinity by 0.3–0.5 psu at depth 50 m, indicative of the stabilization of density by salinity. Horizontal variations of about 0.1 K and 0.15 psu are found over 5-km legs in the mixed layer. The mean vertical shear derived from the Autosub ADCP was about $5 \times 10^{-3}$ s$^{-1}$. Air–water temperature differences are less than ±2 K. Observations described below show that water containing the bubble clouds is slightly colder than the surrounding water, indicating a generally small mean surface heat loss consistent with observed sign of the skewness, $S$, of temperature derivatives (see section 1).

### b. Autosub motion

The Autosub speed over the bottom is derived from postcruise analysis of GPS fixes, and the speed through the water determined from the ADCP. Depth, pitch, and roll sensors show that the vehicle has a natural period of oscillation of about 20-s period. This leads to mean depth variations of about 0.4 m in operations at 2 m in waves with a height, $H_s$, of about 1 m and period of about 3.9 s. Pitching motion changes the orientation of the sonar beams, particularly at depth 2 m when the standard deviation of pitch is 3.4° and forward beam sonographs have, in consequence, changes in intensity and resolution at periods of some 20 s, which sometimes make wave breaking more difficult to identify (see section 3c). In the same sea condition, the waves cause the vehicle to roll with their Doppler shifted periodicity with an rms amplitude of about 2.1° at depth 2 m but this has relatively little effect on the sonographs. Depth, pitch, and roll variations diminish as depth increases and in calmer weather.

### c. Waves; $T_w$ and $H_s$

Dominant wind wave, $T_w$, and swell periods for each leg are estimated from the spectra of the three accelerometers and the pressure transducer in the turbulence package. The mean frequencies at the spectral peaks near wave or swell frequencies are determined from all four sensors and are Doppler shifted, allowing for wave propagation from the wind direction or in the reported swell direction.

Significant wave heights, $H_s$, are derived from a combination of pressure and vertical accelerometer signals. Autosub is almost neutrally buoyant and, although limited by its inertia and finite length (typically 0.3 of a wavelength), tends to move vertically in response to the wave motions. At the frequencies of waves and swell, the vertical accelerometer provides information about the body motion while the pressure signal measures the relative sea surface level. Signals are corrected to allow for Doppler shift and attenuation of the wave signal with depth, integrated and (with acceleration divided by radian frequency squared) added to give an estimate of the rms surface amplitude, $\zeta$. The significant wave heights given in Table 1, estimated as $H_s = 4.0\zeta$ [Massel 1996, p. 141, Eq. (4.131)] are in 20% agreement with those estimated visually from the ship. The largest contribution comes from the accelerations.

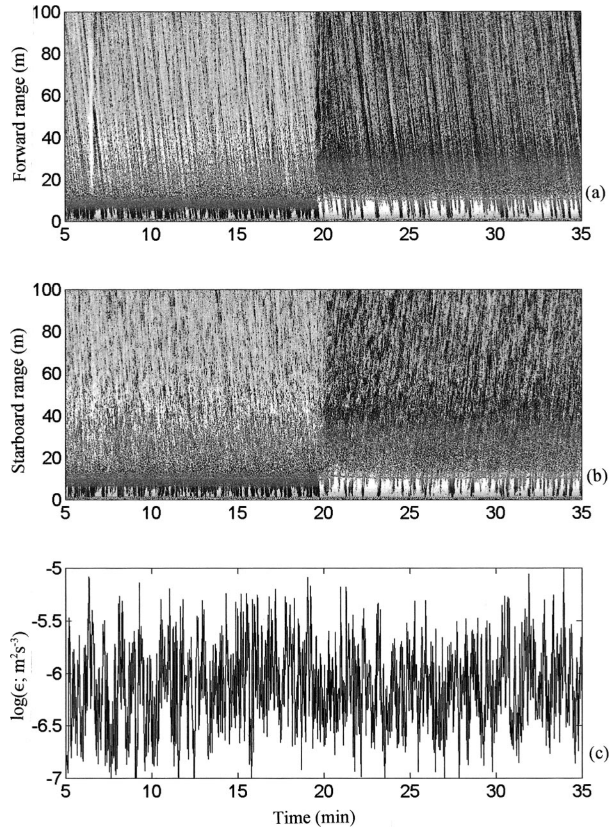


FIG. 1. Thirty-minute (a) forward and (b) starboard sonographs, and (c) log$\epsilon$ with $\epsilon$ in m$^3$ s$^{-3}$, showing a turn and a change in depth from 6 to 10 m at time 20 min. Range is plotted vertically and time horizontally.

### d. Sonographs

Sonographs displaying the intensity of acoustic scattering in time and range coordinates are produced from each of the forward- and starboard-pointing sonar records. Acoustic scattering is recorded as an uncalibrated signal output measured in volts. Data are sampled in a series of range bins, each 0.227 m long, as estimated using a nominal speed of sound of 1500 m s$^{-1}$ and a sampling time of 0.15 ms. No time-varying gain is applied and signal strength diminishes at large range. Correction is made by normalizing the signal, subtracting the mean, and dividing by the standard deviation at each range. This gives a time–range array of zero-mean data with high positive values indicating targets much greater than the mean at a particular range. Further image enhancement is achieved by gray- (or color) scale selection. A set of 1-h-long sonographs were generated immediately following data recovery to confirm the correct operation of the sonars and to check times of legs and dives. These are also useful in providing information about the maximum useful range for further analysis and in confirming the wind direction.

Figure 1 shows sonographs of a 30-min period. At about time $t$ = 20 min, there is a 90° change in course from 331° to 241° and a change in Autosub depth from 6 to 10 m. The acoustic targets are the dark bands in the forward (Fig. 1a) and starboard (Fig. 1b) sonographs. At short ranges, both sonographs show the bubble clouds below the surface. The forward sonograph shows targets, bubble clouds, which decrease in range as time increases at a rate equal to the speed of the vehicle relative to acoustically reflecting clouds. The wind speed is about 12 m $s^{-1}$ from 110° so that, before the turn, bubble bands aligned in the wind direction by Lc are orientated at 41° to the left of the Autosub track and after the turn are 49° to the right. In consequence the bands visible in the starboard sonograph decrease in range before the turn and recede after it. Shadowing causing a white vertical band with little signal return can be seen in Fig. 1a at about $t = 7$ min caused by an intensely scattering bubble cloud. In both parts of the record signals are poorly defined between the surface and about 20 m. This loss of resolution is typical of sonographs in higher winds and probably derives from intense specular reflection from the sea surface at the lower incidence angles. Figure 1c illustrates the highly variable turbulent dissipation rate, $\epsilon$, plotted here on a log scale.

### *e. Bubble clouds*

Bubble clouds through which the Autosub is passing are identified and characterized using the voltage $V_8$ measured at range bin 8 of the starboard sonar, about 1.1 m above the level of the turbulence probes. This distance is at best a rough approximation since the sonar beam has a width of 33° in the vertical, sidebands exist, and signal returns may be biased toward stronger signals at shallower depths. A ''threshold'' level, $V_8 = 6.76$ v, is selected to provide a basis on which to identify and quantify the dimensions of bubble clouds. Values exceeding this threshold are recognized as bubble clouds. This arbitrary signal threshold is equated to an acoustic scattering cross section, $\mathrm{Mv} = (3.0 \pm 0.9) \times 10^{-4}\ \mathrm{m}^{-1}$, by comparing the mean $V_8$ values at known depths and wind speeds with measured scattering cross sections found by Thorpe (1982) at the same depths and wind speeds.[1]

### *f. Breaking waves*

Breaking waves produce shortlived strongly scattering features visible in the forward sonographs signals that are used to identify the time delay before the location of wave breaking is crossed by Autosub. This information is used to assess the rate of dissipation of turbulence produced by the breakers at known times after their breaking (section 3c).

[1] The selected threshold is between that of $\mathrm{Mv} = 6 \times 10^{-5}\ \mathrm{m}^{-1}$ used by Thorpe (1986b) and $10^{-3}\ \mathrm{m}^{-1}$, the lower of the values adopted by Thorpe and Hall (1987).

### *g. Wind-aligned bubble bands and Langmuir circulation (Lc)*

Figures 2a, b show 6-min forward and starboard sonographs with bands of bubbles, characteristic of the convergence regions of Lc. Figure 2b shows that the bands are not uniform, continuous, regular, and parallel, but consist of lines of bubble clouds of various scattering strength, which writhe and twist in space, symptomatic of their unstable nature, while remaining, on average, roughly aligned with the wind (see also Farmer and Li 1995). A method for identifying such persistent and extensive bands was devised to allow rapid semiobjective analysis of the large dataset. For each 2-Hz sonar pulse, the *normalized* signals from the forward sonograph (e.g., Fig. 2a) are scanned along directions corresponding to speeds close to that of the Autosub through the water. If the direction having the maximum fractional number of points with value >0.5 (i.e., with more than 0.5 standard deviations from the mean) exceeds 0.6 and consequently has a relatively high persistence in the record, the time is registered as that of a potential Langmuir band. The criterion implies that bands are detectable in the forward sonar for about 60 s. Confirmation is sought by analysis of the corresponding starboard sonograph. By simple geometry, a band that is aligned with the wind in direction $\theta$ has a tilt, $dr/dt = \upsilon \tan(\theta - \phi)$ in the starboard sonograph, where $r$ is the range of the band, $t$ is time, and $\upsilon$ and $\phi$ are the Autosub speed through the water and course direction, respectively. At the registered times, a scan is made in the starboard sonograph over a range of $(\theta - \phi)$ from $-25°$ to $+25°$ of the effective wind direction, and the maximum fractional coverage found. Because of the high variability in bubble band concentration and position, only a mean signal level of 0.5 and a lower fractional coverage of 0.5 between 20 and 50 m are demanded for acceptability. Typically this implies that lengths of about 70 m are required to meet the detection threshold as the Autosub converges with bands.

### *h. Conditional sampling*

The analysis described below relies on conditional sampling. The times at which one measured quantity, the ''conditional quantity'' (e.g., acoustic scattering) is exceptionally large or ''extreme,'' are used to fix times of physical ''events'' (e.g., a high population of acoustically scattering bubbles). Separate averages are then made (in 0.5-s bands) of the conditional quantity and of others (e.g., dissipation and temperature) out to 20 s on either side of the selected times of the events, to generate average time ''sections'' of quantities across events in the selected conditional quantity. The averaging serves to remove noncoherent signals (e.g., those produced by surface waves) except where these are phase linked to conditional quantities. The time sections can be converted into distance using the mean Autosub

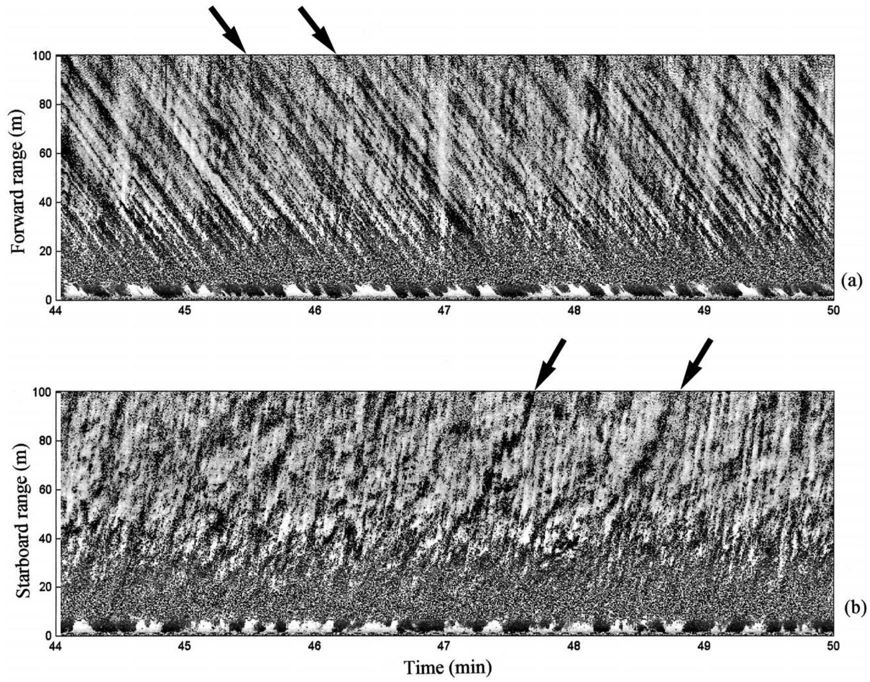


FIG. 2. An example of 6-min sonograph records with bubble bands caused by Langmuir circulation: (a) forward sonograph and (b) the corresponding starboard sonograph. Two bubble bands ascribed to Langmuir circulation are marked by arrows.

speed (about 1.25 m s$^{-1}$). Earlier studies (e.g., Thorpe and Hall 1987; Gemmrich and Farmer 1999b) prove this to be a useful and successful means of extracting signal from strong background noise.

## 3. The observations

### a. Dissipation rate, $\epsilon$

Table 2 lists statistical values of dissipation rate $\epsilon$, $z/H_s$, and wave age $c/u_*$. Figures 3a, b show the variation of $\log(kz\epsilon_m/u_{*w}^3)$ with mean nondimensionalized depth, $z/H_s$, and the wave age, $c/u_*$ based on leg-average values of dissipation rate, $\epsilon_m$. Values of $z/H_s$ range from 1.55 to 13.65. In steady winds with $c/u_* \approx 14$, $\epsilon_m$ follows the law of the wall [Eq. (1); $kz\epsilon_m/u_{*w}^3 \approx 1$] with no significant variation of $kz\epsilon_m/u_{*w}^3$ with $z/H_s$. Values of $\epsilon_m$ significantly exceed the values of (1), however, in the conditions of swell and decreasing winds with $c/u_* > 20$.

The observed inverse proportionality of $\epsilon_m$ with depth $z$ means that changes $\Delta\epsilon$ in $\epsilon_m$ correspond to changes $\Delta z$ in $z$ with $\Delta\epsilon/\epsilon_m = -\Delta z/z$, implying a vertical advective scale of dissipation, or ''mixing length,''

$$\Delta z = |z\Delta\epsilon/\epsilon_m|, \tag{3}$$

at depth $z$. This is used later to characterize the mixing associated with bubble clouds, Langmuir bubble bands, and temperature ramps. The mean vertical displacements of Autosub, $\Delta d$, when passing through these features are much less than $\Delta z$.

Histograms of $\log\epsilon$ at depths of 2, 4, 6, and 10 m in mean winds of 11.6 m s$^{-1}$ are shown in Fig. 4a. The dissipation rate is closely lognormal; mean skewness and kurtosis are close to zero and 3, respectively. The wavenumber spectra of dissipation rate in mean winds of 11.6 m s$^{-1}$ derived using the Taylor frozen field hypothesis have a mean slope, $p = -0.61 \pm 0.07$ in the wavelength range from 5 to 50 m, while the temperature frequency spectra have a more conventional $-5/3$ slope in the range 0.02–10 Hz, (0.1–60 m), with no significant variation of spectral energy levels with depth between 2 and 10 m or peaks that might indicate the presence of regular Lc bands.

### b. Variation of $\epsilon$ and temperature in bubble clouds

At depths of 2–4 m the majority of peaks in $\epsilon$ can be identified with features in the forward sonograph record, either with clouds that persist for more than 80 s as the Autosub approaches, many of which are Lc bands, or bubbles left from breakers. Histograms of bubble cloud ($V_8 \geq 6.76$ v) lengths decay approximately exponentially with cloud length $l$. The probability, $p(l)$, of clouds of length $> 1.25$ m is proportional to $\exp(-ql)$, where $q$ is a constant that increases with depth and decreases with wind speed. Values typically 20% higher than those of the exponential relationship are found for cloud lengths $<1.25$ m. The mean lengths of bubble clouds decreases with depth, being 7.3, 4.2, 2.7, and 1.1 m at mean depths of 2.09,

TABLE 2. Dissipation-related values and statistics. The table columns, left to right, list mission/leg (as in Table 1), nondimensionalized depth $z/H_s$, mean dissipation ($\epsilon_m$) over the legs ($10^{-6}$ m$^2$ s$^{-3}$ = $10^{-6}$ W kg$^{-1}$), the skewness of log$\epsilon$, kurtosis of log$\epsilon$, $kz\epsilon/u^3_{*w}$, and wave age $c/u_*$, where $c$ is found from the dispersion relation, $c$ (m s$^{-1}$) = $1.56T_w$ (s), and $T_w$ is the wave period given in Table 1.

| Mission Leg | $z/H_s$ | Avg dissipation $\epsilon_m \times 10^6$ (m$^2$ s$^{-3}$) | Skewness of log$\epsilon$ | Kurtosis of log$\epsilon$ | $\epsilon kz/u^3_*$ | $c/u_*$ |
|---|---|---|---|---|---|---|
| 1.1 | 2.06 | 3.28 | −0.017 | 2.88 | 0.58 | 12.5 |
| 1.2 | 2.37 | 3.01 | −0.156 | 2.68 | 0.96 | 15.2 |
| 1.3 | 4.48 | 2.03 | −0.131 | 3.03 | 0.91 | 13.9 |
| 1.4 | 4.23 | 1.77 | −0.101 | 2.59 | 0.66 | 13.2 |
| 1.5 | 4.83 | 1.47 | −0.132 | 2.71 | 1.12 | 14.5 |
| 1.6 | 7.02 | 1.06 | −0.030 | 2.64 | 0.68 | 13.7 |
| 1.7 | 11.13 | 1.16 | −0.041 | 2.79 | 0.83 | 11.9 |
| 1.8 | 9.97 | 1.22 | −0.061 | 2.84 | 1.27 | 13.4 |
| 1.9 | 3.46 | 1.98 | −0.134 | 2.75 | 0.81 | 13.6 |
| 1.10 | 4.66 | 2.30 | −0.181 | 2.91 | 0.82 | 12.9 |
| 1.13 | 13.65 | 1.08 | 0.072 | 2.97 | 0.98 | 12.9 |
| 1.14 | 15.88 | 0.67 | 0.177 | 2.99 | 1.16 | 16.0 |
| 1.15 | 2.37 | 1.80 | −0.136 | 2.74 | 0.75 | 17.4 |
| 1.16 | 2.16 | 2.20 | −0.178 | 2.85 | 0.60 | 14.9 |
| 1.17 | 11.00 | 1.28 | 0.182 | 2.78 | 3.37 | 18.4 |
| 2.1 | 2.61 | 1.02 | −0.035 | 2.89 | 0.81 | 16.9 |
| 2.2 | 2.55 | 1.14 | −0.161 | 2.66 | 0.89 | 16.9 |
| 2.12 | 3.17 | 0.29 | 0.104 | 3.00 | 1.31 | 21.2 |
| 2.13 | 6.67 | 0.17 | 0.141 | 3.00 | 0.75 | 27.1 |
| 2.14 | 9.85 | 0.13 | 0.515 | 3.83 | 1.24 | 30.8 |
| 2.15 | 17.85 | 0.14 | 0.660 | 3.71 | 2.51 | 34.2 |
| 3.1 | 3.69 | 0.73 | −0.241 | 2.77 | 1.41 | 24.5 |
| 3.2 | 3.84 | 1.20 | −0.360 | 2.91 | 2.88 | 26.3 |
| 3.3 | 5.29 | 0.51 | 0.197 | 3.17 | 3.95 | 27.5 |
| 3.4 | 25.63 | 0.61 | −0.338 | 3.29 | 7.89 | 32.7 |
| 3.5 | 41.19 | 0.30 | 0.117 | 2.70 | 11.52 | 38.5 |
| 3.6 | 41.17 | 0.11 | 0.110 | 2.79 | 7.97 | 43.8 |
| 4.22 | 1.58 | 6.38 | 0.006 | 2.73 | 0.92 | 15.2 |
| 4.23 | 1.55 | 5.78 | −0.041 | 2.69 | 0.90 | 14.2 |
| 4.24 | 5.46 | 2.23 | −0.039 | 2.65 | 1.16 | 15.8 |
| 4.25 | 7.18 | 2.15 | −0.006 | 2.93 | 1.13 | 17.1 |
| 4.26 | 4.23 | 2.42 | −0.016 | 2.69 | 0.58 | 13.1 |
| 4.27 | 3.10 | 2.22 | −0.042 | 2.80 | 1.01 | 14.0 |
| 4.28 | 12.72 | 1.03 | 0.303 | 2.71 | 1.10 | 15.0 |

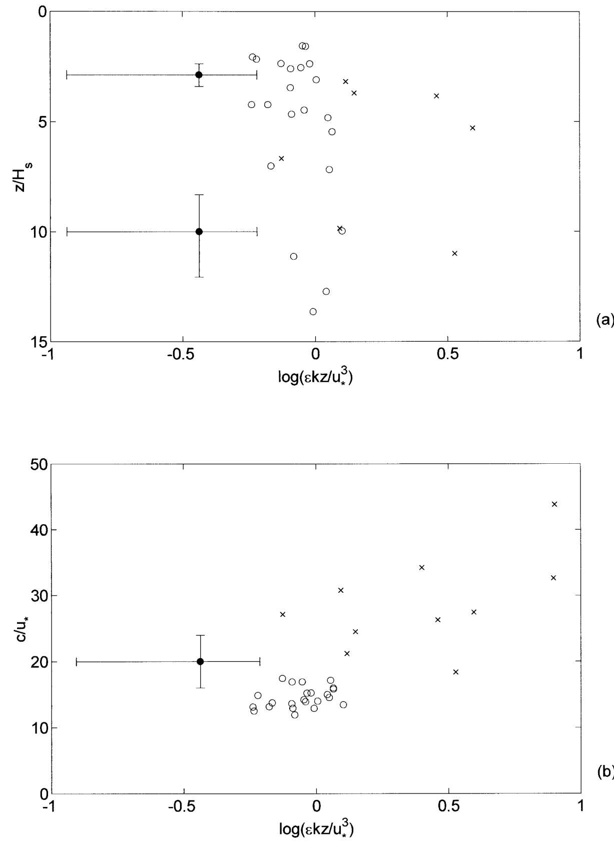


FIG. 3. The variation of log($k\epsilon_m z/u^3_{*w}$) with (a) $z/H_s$ and (b) the wave age $c/u_*$, where $\epsilon_m$ is the mean value of $\epsilon$, and $z$ is the mean depth averaged over a leg. Values shown by circles (o) are for steady winds (mission 1, legs 1–16, and mission 4, legs 22–28). Values with crosses (x) are from other legs when wind speed is decreasing and swell is present (see Table 1). Error bars are shown. The estimates are dominated by the uncertainty of about 50% in $\epsilon_m$ and by a 20% uncertainty in $H_s$.

4.04, 6.1, and 10.43 m, respectively, in mean winds, $W_{10}$, of 11.6 m s$^{-1}$. Correlation lengths are 1.2, 0.89, and 0.67 m at depths of 2.91, 3.78, and 5.76 m, respectively, when $W_{10}$ = 4.7 m s$^{-1}$. These values accord with the known decrease in the mean acoustic scattering cross section as depth increases or wind decreases. The mean length of the gaps between clouds increases with depth (1.7, 3.2, 5.5, and 57 m, respectively) in mean winds of 11.6 m s$^{-1}$.

There is a notable tendency for high values of $\epsilon$ to occur within bubble clouds. Histograms of values of log$\epsilon$ measured within bubble clouds are superimposed in black on the log$\epsilon$ histograms for all data in Fig. 4a. Although the distribution of log$\epsilon$ in bubble clouds remains close to normal, its distribution is shifted toward higher values. Consequently the fraction, $F$, of dissipations rates that lie within bubble clouds (Fig. 4b) increases as log$\epsilon$ increases. At depth 2.1 m in winds of 11.6 m s$^{-1}$, more than 80% of the values of log$\epsilon$ which exceed its mean value are in bubble clouds, and more than 95% of those exceeding the mean plus two standard deviations are in bubble clouds. At 3.9 m, more than 62% of the log$\epsilon$ values that exceed the mean are in bubble clouds, while more than 82% of those exceeding the mean by more than two standard deviations are in bubble clouds. The percentage values decrease as depth increases as the fractional horizontal extent of bubble clouds decreases, but at 5.95 m more than 60% of values that exceed mean log$\epsilon$ by more than two standard deviations are in bubble clouds, indicating the connection of high dissipation rate and turbulent motion with processes at the sea surface. Consequently at shallow depths most of the turbulent dissipation occurs in bubble clouds; the ratio of the total dissipation rate in clouds to the total dissipation rate is 0.85, 0.67, 0.41, and 0.071 at mean depths $z$ =

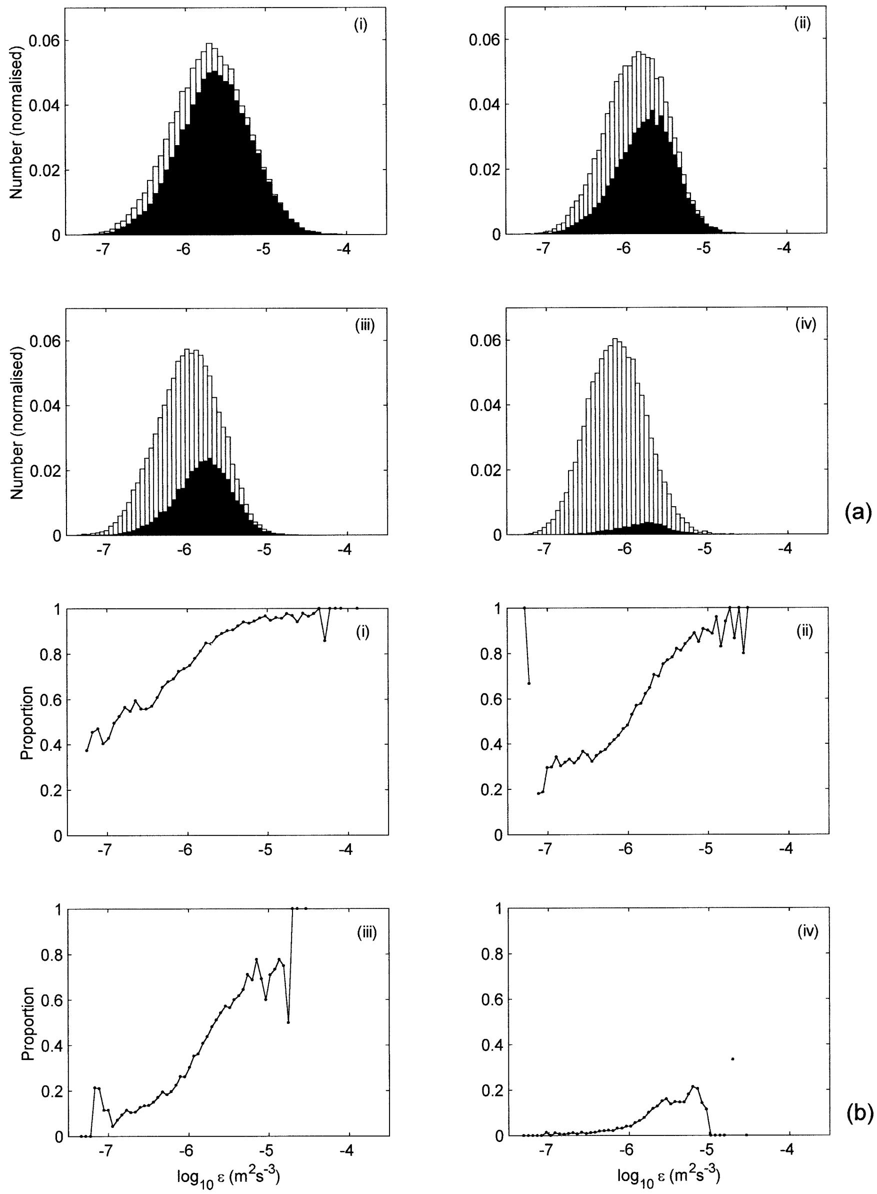


FIG. 4. The variation of log$\epsilon$ in winds averaging 11.6 m s$^{-1}$. (a) Histograms of log$\epsilon$ with $\epsilon$ in m$^2$ s$^{-3}$, in the full record and (superimposed in black) only within bubble clouds where acoustic scattering cross section exceeds $(3.0 \pm 0.9) \times 10^{-4}$ m$^{-1}$ at mean depths of (i) 1.93, (ii) 3.90, (iii) 5.95, and (iv) 10.4 m. (b) Ratio of histograms shown in (a) at the same four mean depths, (i)–(iv). Many of the high dissipation values occur in bubble clouds, especially at the shallower depths.

2.10, 3.90, 5.95, and 10.37 m (or $z/H_s$ = 1.92, 4.35, 6.41, and 11.77), and mean wind speeds of 10.6, 11.9, 11.6, and 11.7 m s$^{-1}$, respectively, all exceeding the fraction of run length for which bubble clouds are present, 0.79, 0.60, 0.32, and 0.053, respectively. The ratio of the mean dissipation rate in bubble clouds to the average dissipation, $\epsilon_m$, at each depth increases with depth, being 1.12, 1.23, 1.41, and 1.75, respectively, in the same conditions. Using (3), the mean differences between $\epsilon$ in clouds and the averages, $\Delta\epsilon$, gives a mean mixing length, $\Delta z$, of 0.4, 1.0, 2.2, and 6.0 m in the same mean depth and wind speed ranges.

Higher values of $\epsilon$ occur in bubble clouds of greater horizontal extent (possibly those created by the strongest breakers) and correspondingly lower values in longer gaps. For example, at 3.9 m in winds of 11.6 m s$^{-1}$, bubble clouds shorter than 4.4 m have lower than leg-average dissipation rates, $\epsilon_m$, and those longer have greater dissipation rates, $\epsilon$, while the mean $\epsilon$ in all clouds deeper than 4 m are greater than $\epsilon_m$ at their respective

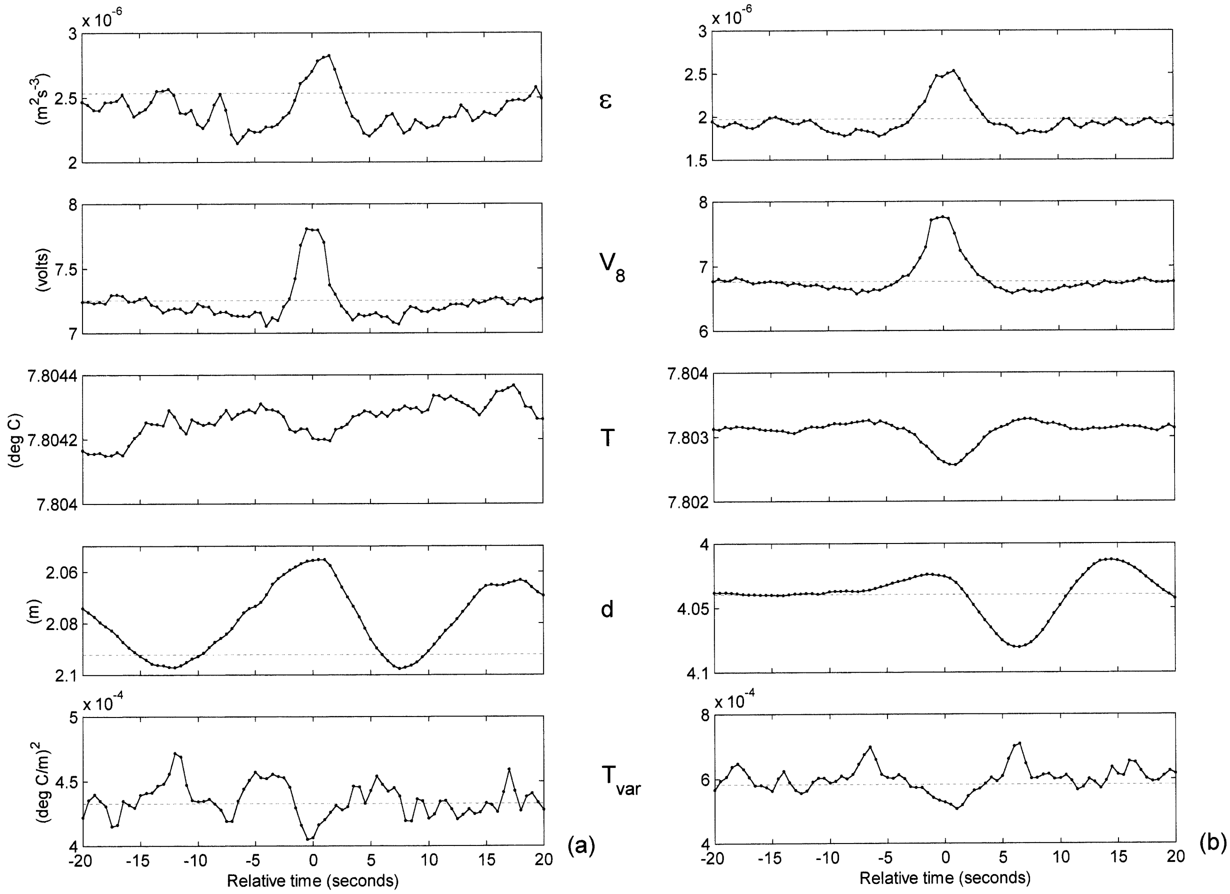


FIG. 5. Conditional sample plot at times of the center of bubble clouds [acoustic scattering cross section exceeds $(3.0 \pm 0.9) \times 10^{-4}$ m$^{-1}$] longer than 2 s (2.5 m) in extent along the Autosub track at 45° to the wind direction in which at mean depths of (a) 2.09 m (1400 samples), (b) 4.04 m (1289 samples), (c) 6.10 m (356 samples), and (d) 10.43 m (108 samples). Parts in each are, top to bottom, dissipation rate ($\epsilon$),

levels. Correspondingly, the mean $\epsilon$ in gaps between clouds is less than 75% of $\epsilon_m$ at 2.1 m and less than the mean in gaps exceeding 3.2 and 11 m at 3.9 and 5.95 m, respectively.

Figure 5 shows conditional sample plots about the center of bubble clouds longer than 1.9 m (1.5 s) or about 0.11 times the wavelength of the dominant waves. Mean depths increase from Fig. 5a to Fig. 5d. The Autosub track is at about 45° to the wind direction. Dissipation rates near the center of the clouds (top panels at each depth) are seen to reach values about 25% higher than the mean (shown as horizontal dashed lines.) The bubble clouds indicated by acoustic scattering, $V_8$, broaden with depth (second panels) and so does the temperature $T$ in the clouds (third panels), which is depressed by about 1 mK. The depth $d$ of the Autosub (fourth panels) increases at rates of $1 \pm 0.5$ cm s$^{-1}$ as, or soon after, it passes through clouds, consistent with there being a downward motion, and oscillates afterwards with a period corresponding to that set by the mechanical control of the vehicle, about 20 s. At all depths, however, $d$ decreases as clouds are approached, indicating an upward motion. The temperature at depth 4.04 m (Fig. 5b) rises both before and after the average bubble cloud is crossed. This signal becomes more pronounced when clouds are categorised according to length. Figure 6, for example, shows a conditional sample plot at the same depth but restricted to clouds of 8 s (10.0 m) length. These have enhanced dissipation over most of the cloud area, a reduction in $\epsilon$ on either side, and a clear rise in $T$ on each side of the cold cloud of bubbles. As will be shown in section 3d, these features are consistent with the clouds being dominated by the pattern of flow associated with Lc. The clouds are sites of diminished variation in mean square temperature gradient, $T_{var}$, (bottom panels of Fig. 5 and 6), suggesting they are relatively well mixed by the enhanced turbulence.

## c. Turbulence from breaking waves

Two-minute sonographs from the forward-pointing sonar and corresponding measurements of $\epsilon$ are shown in Fig. 7. At smallest range an indistinct horizontal line of scatterers can be seen within the sonar Fresnel zone. Beyond are subsurface bubble clouds that ap-

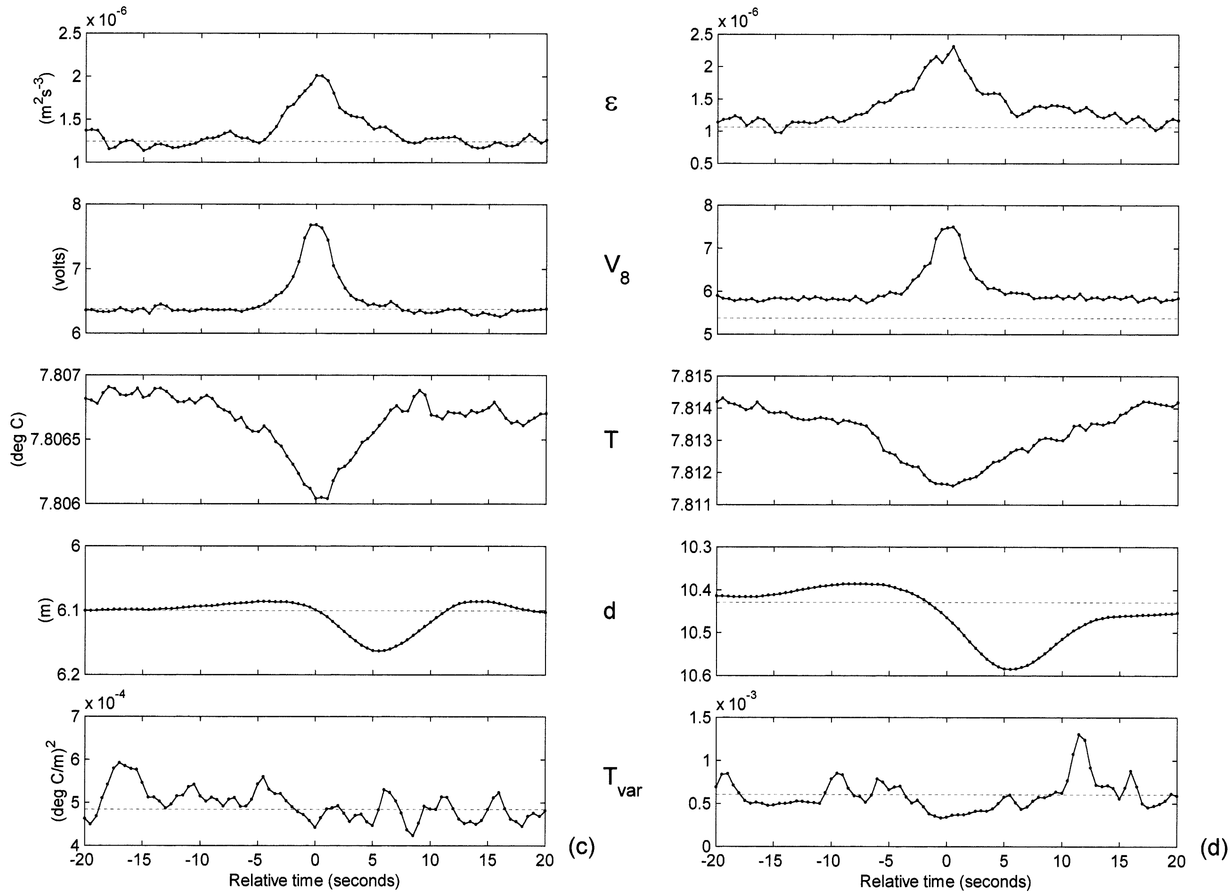


FIG. 5. (*Continued*) acoustic scattering voltage ($V_8$), temperature ($T$), depth ($d$), and temperature variance ($T_{var}$). Data were obtained along tracks at 45° to the mean winds of 11.6 m s$^{-1}$. Mean values are shown by horizontal dashed lines.

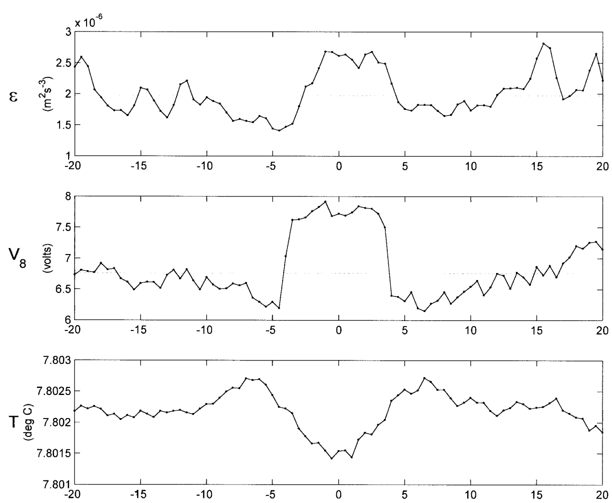


FIG. 6. Conditional sample plot at times of the center of 51 bubble clouds of 8-s (10 m) length at a mean depth of 4.04 m in mean winds of 11.8 m s$^{-1}$ showing, top to bottom, dissipation rate ($\epsilon$), acoustic scattering ($V_8$), and temperature ($T$). Data were obtained along tracks at 45° to the mean winds. Mean values are shown by horizontal dashed lines.

pear tilted because they are being approached by Autosub and viewed in the forward sonar beam. The water surface and waves are occasionally detectable at a range equal to the Autosub depth. At ranges between this and about 15–20 m in records at higher winds is the second region of ill-defined targets referred to in section 2d, apparently resulting from strong reflection from the water surface almost above the vehicle. At larger ranges are

1) almost vertical and periodic bands resulting from specular reflection from approaching waves (e.g., near a time of 20 min in Fig. 7a. These are best seen by viewing the figure from below at small angle to the page);
2) bands that change range at about 1.25 m s$^{-1}$, almost stationary clouds of bubbles being approached by the Autosub; and
3) short strong (black) reflections, marked by arrows, from highly scattering, intense bubble clouds produced by waves breaking ahead of Autosub. (These should not be confused with the vertical lines about 20 m long at ranges beyond 60 m which are caused by interference from the Autosub ADCP and are

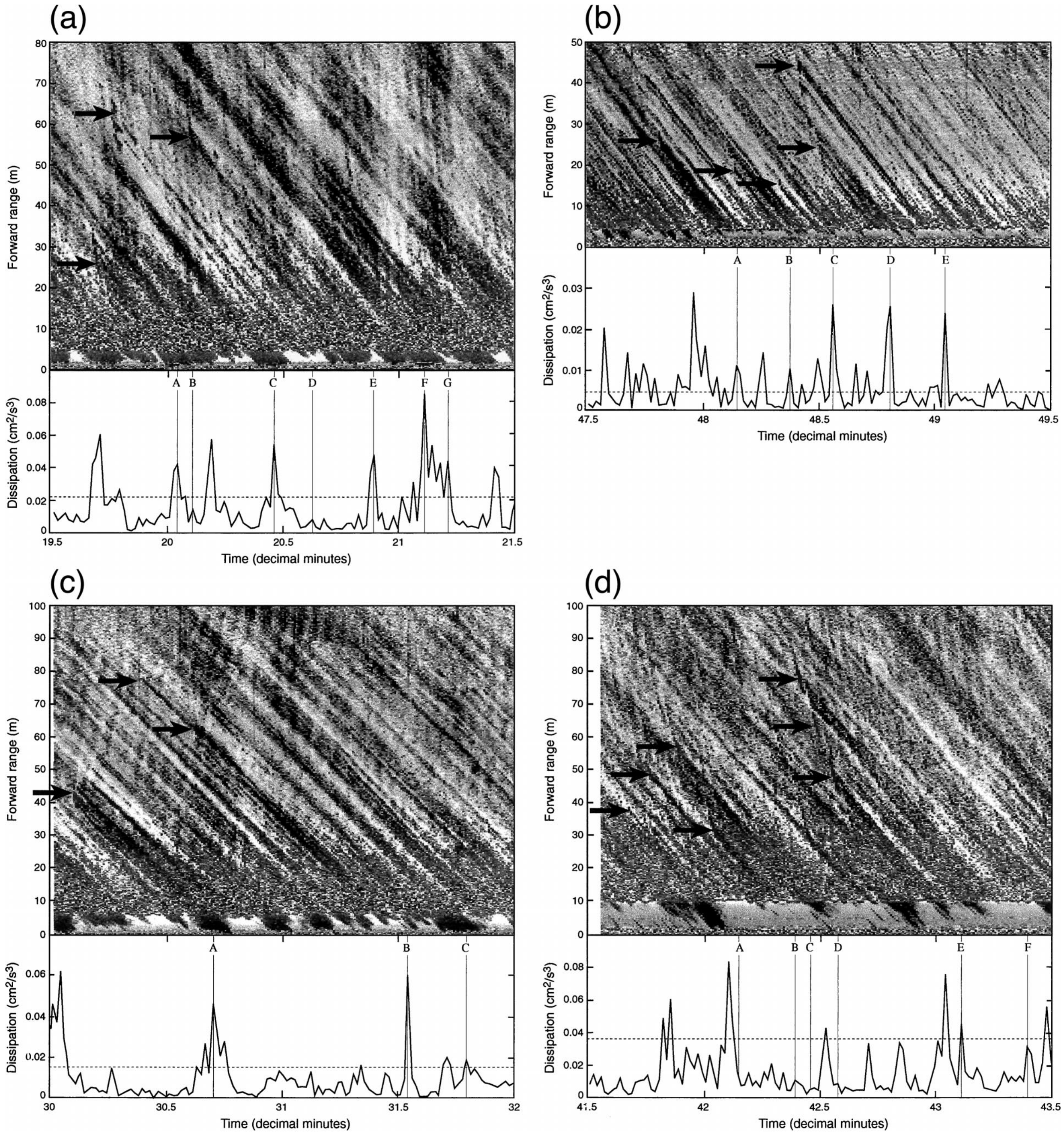


FIG. 7. Examples of forward sonograph records in which breaking waves and the consequent bubble clouds are visible (above) and associated dissipations, $\epsilon$ (below, cm$^2$ s$^{-3}$), with the mean leg dissipation marked by a dashed line: (a) from mission 1, leg 4 at depth 4 m, $W_{10}$ = 11.8 m s$^{-1}$; (b) from mission 3, leg 3 at 4 m, $W_{10}$ = 5.0 m s$^{-1}$, (c) from mission 1, leg 6, at 6 m, $W_{10}$ = 11.3 m s$^{-1}$; (d) from mission 1, leg 17 heading into wind at 10 m, $W_{10}$ = 10.0 m s$^{-1}$; and (e) from mission 1, leg 7 at 10 m, $W_{10}$ = 12.8 m s$^{-1}$.

artifacts.) The breakers are sources of bubble clouds lasting for typically 1 min which, in the sonograph time-range display, appear as inclined bands of scatterers emanating from the breaker location. Their locations at zero range serve to identify the times at which Autosub passes through a previous breaker position.

These times were carefully measured for a total of about 950 breaking waves, together with the ‘‘age’’ (the time since turbulence was generated by a breaker) of the turbulent patch when sampled. Measured ages range from 10 to 80 s. The dissipation rate in the regions of past breakers at known time delays after breaking is then found from the time series of $\epsilon$, as indicated by the lines

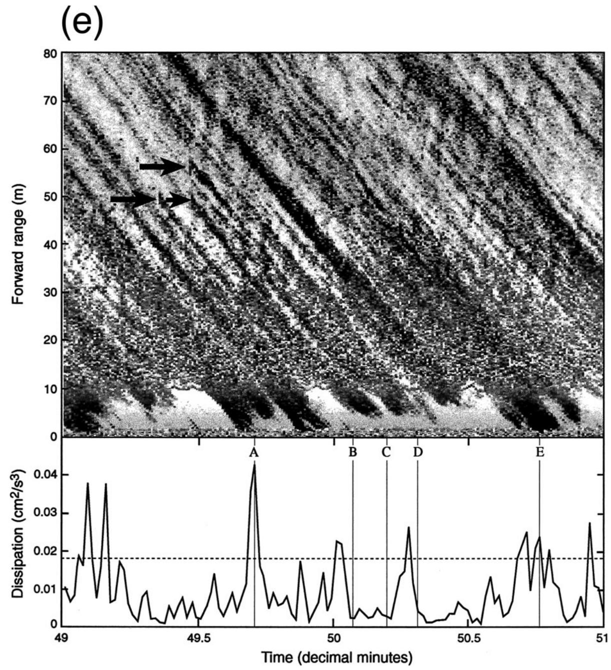


FIG. 7. *(Continued)*

superimposed on Fig. 7. It proves difficult to identify breakers in the forward sonographs at an Autosub depth of 2 m because of the vehicle's pitching and because of the shadowing of breaking events by bubble clouds near the Autosub. Targets are masked by the surface ''stratus'' layer of bubbles that forms beneath the surface at wind speeds greater than about 7 m s$^{-1}$, making the detection of breakers at wind speeds of about 12 m s$^{-1}$ or more very difficult (Thorpe and Hall 1983), a problem compounded at 2 m because of the vehicle's pitching. Only features with a clear strong breaking wave with subsequent strong bubble targets and that do not occur in a preexisting bubble band are selected for analysis.

Three breakers or breaker groups are indicated in Fig. 7a at an Autosub depth of about 4 m and $W_{10} = 11.9$ m s$^{-1}$. The earliest result in a peak in $\epsilon$ at A, exceeding the leg mean, some 20 s after the breaking occurred. A relatively small dissipation rate is associated with the second breakers (D), although the peak at C may be the consequence of a breaker at smaller range which occurs slightly earlier. The third breaker results in an $\epsilon$ peak (E). Other $\epsilon$ peaks (F–G) are associated with an intense bubble cloud persisting for more than 50 s and already visible at maximum range, perhaps a band caused by Lc.

Figure 2b is also at depth 4-m but at lower wind speed, $W_{10} = 5$ m s$^{-1}$. Several breakers are evident, some marked by arrows, and with each there is an $\epsilon$ peak. The first and apparently most intense, at A, produces relatively moderate $\epsilon$, less than that of the more distant breaker at E. The latter shows a common feature, two lines separated by about 1 m from what appears to be a single breaker. It is impossible to know whether this is a consequence of multiple breaking or a separation of the bubble clouds induced in the three-dimensional structure and subsequent circulation induced by a single breaking event.

Figure 7c at depth 6 m has three breakers marked by arrows. The first, possibly multiple breaking, leads to a broad $\epsilon$ peak at A. The other two waves break in the same location, although about 10 s apart in time, and result in a large $\epsilon$ peak at B. The $\epsilon$ peak at C is in a large bubble cloud possibly caused by breakers at time about 30.6 min and range 90 m, but has relatively low $\epsilon$. None of the breakers shown in Fig. 7d at depth 10 m lead to $\epsilon$ peaks exceeding the leg mean. The first (A), about 30 s after breaking, has $\epsilon$ which is only about a quarter of the mean for the leg. The next three breakers also lead to relatively small $\epsilon$ (B–D). The last three arrows near time 42.5 min mark a set of waves breaking sequentially in a group (see Thorpe and Hall 1983). Repetitive breaking is more apparent, as here, in legs heading directly into the wind. Dissipation rates associated with breakers B–D in Fig. 7e, also at 10 m, are again small, although there are relatively high values of $\epsilon$ in deep bubble clouds (possibly in Lc bands), notably at A and E.

It had been hoped to estimate the mean variation in $\epsilon$ with time after wave breaking, as a function of depth. In the steady winds of about 11.6 m s$^{-1}$ it is not however possible to identify a breaker closer than about 25 m ahead of the Autosub and the breaker zone is consequently not sampled until at least 20 s or about five wave periods after the breaking event. Dissipation rates are therefore only measured in identifiable breakers at a time after that in which most of the turbulent decay has already occurred in laboratory experiments. A total of 72, 80, 52, and 104 breakers were examined at depths 2.09, 4.04, 6.10, and 10.43 m, respectively, from measurements in Autosub tracks at about 45° to the wind. The mean dissipation rates at 2.09 m increase by about 50% between time delays of 30 $\pm$ 10 s and 50 $\pm$ 10 s after breaking, but subsequently decrease, reaching values about 80% of the values at 20 s at times of 70 $\pm$ 10 s. There is also a horizontal alongtrack spreading of the high $\epsilon$ regions from a mean of about 4 m at 30 $\pm$ 10 s to about 5 m at 65 $\pm$ 15 s. At depth 4.04 to 10.4 m dissipation rates all show a gradual increase, averaging 17% between 35 $\pm$ 5 s and 65 $\pm$ 5 s time delays. The standard deviations of dissipation rates in breaker zones at 2.09 m is also large, about 2.6 times that of the mean.

### *d. Dissipation rates and temperature in Langmuir circulation bands*

Figure 8 shows conditional sample plots centered on bubble bands (see section 2g) in mean wind speeds of 11.6 m s$^{-1}$. The time series are extracted from data rearranged and averaged together so that bands are crossed in a direction from right to left facing upwind

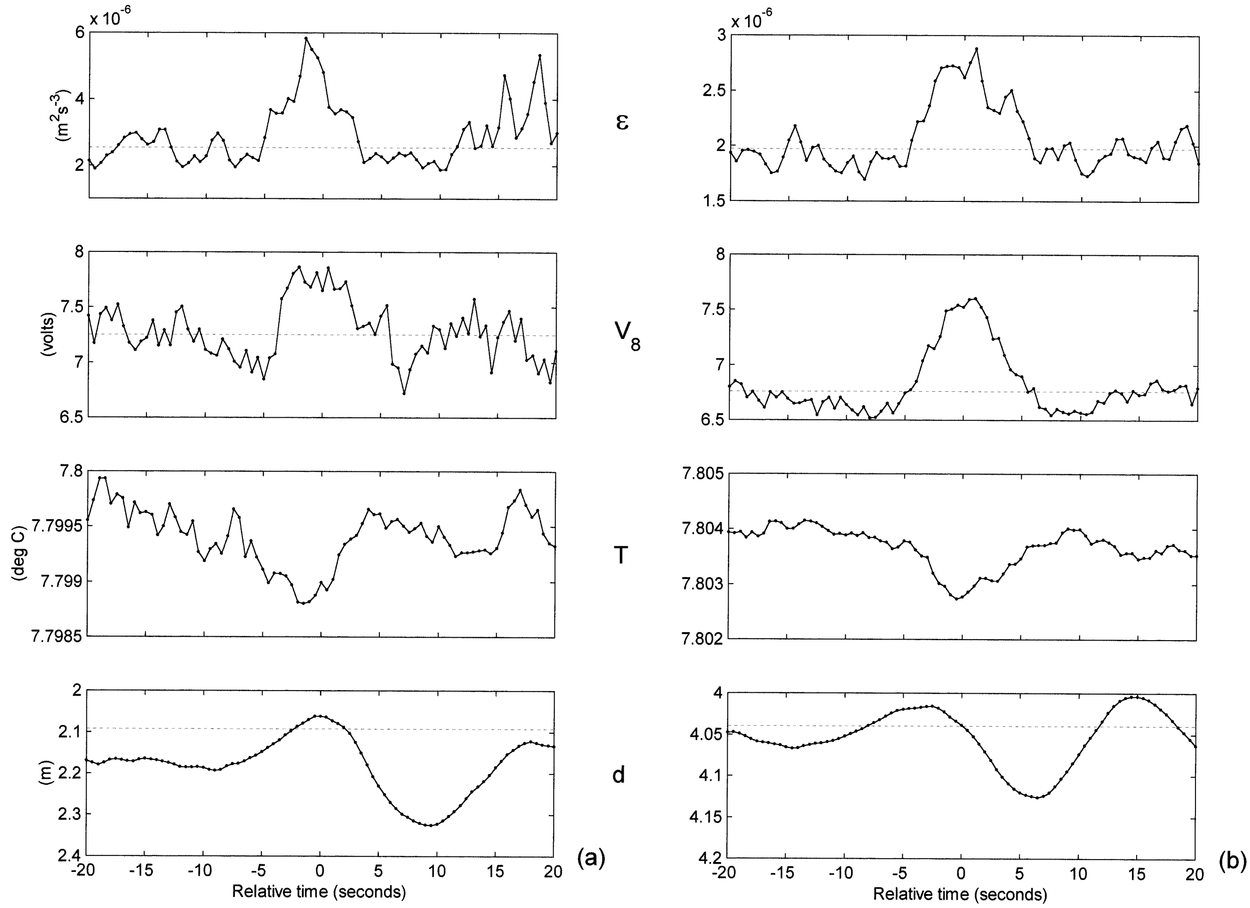


FIG. 8. Conditional sample plot across Langmuir circulation bands in a mean wind speed of 11.6 m s$^{-1}$ at mean Autosub depths of (a) 2.07 m (31 samples), (b) 4.04 m (154 samples), (c) 6.10 m (96 samples), and (d) 10.43 m (294 samples). The panels show, top to bottom,

and in an average direction of about 45° to the wind. The across-wind separation of bands passing the selection criteria is of order 70 m, far greater than the separation of Langmuir cells in the hierarchy of cell sizes that were probably present. The characteristics are similar to those across the bubble clouds but the acoustic scattering is more variable, particularly at depth 6–10 m. Peak average dissipation rates in the bands (top panels) exceed the average values (dashed) by factors of 2.3, 1.35, 1.28, and 1.22 at mean depths $z$ = 2.10, 3.90, 5.95, and 10.4 m ($z/H_s$ = 1.92, 4.35, 6.41, and 11.8), and winds of 10.6, 11.9, 11.6, and 11.7 m s$^{-1}$, respectively, and when $13.5 \leq c/u_* \leq 15.7$. There is, however, evidence of double peaks in $\epsilon$ at depth 6 and 10 m (top panels of Fig. 8c,d). The band widths determined from $\epsilon$, $V_8$ (second panels) and the less well defined lowered temperature in the bands (third panels) all increase with depth; bands are about 5.6, 7.1, 8.5, and 9.9 m wide, respectively, at the four depths with allowance being made for the angle at which the bands are crossed. Autosub depth $d$ (fourth panels) increases slightly as the vehicle crosses the bands, consistent with the downward flow in Lc. The rates of depth increase are 5.7, 2.0, 1.0, and 0.6 cm s$^{-1}$, respectively, more rapidly at depths down to 4 m than in bubble clouds generally. Given the length of the vehicle (7 m) it is not possible to convert these directly into vertical flow speeds, but their magnitude indicates relatively higher downward speeds at shallower depths. It is notable that the relative time location at which the rate of change of depth is zero before such depth increases commence becomes more negative (earlier) as depth increases, about 7 s earlier at a depth of 10 m.

The criteria of section 2g selects only clearly defined linear arrays of bands at ranges *beyond* that of the water surface, not at a depth close to the Autosub. Bands are patchy, and the proportion of bands which contain bubble clouds ($V_8 \geq$ 6.76v) at their centres as Autosub passes through are 94%, 87%, 51%, and 11% at nominal depths 2, 4, 6, and 10 m, respectively. Although the analysis of the formation of bubble bands by Lc (Thorpe 1984) shows that bubble clouds delineate the core of the downward-going flow in the Lc pattern, bubbles rise and only the smallest, with rise speeds less than the downward flow, are trapped by the circulation and carried to depth. This implies that, at the greater depths,

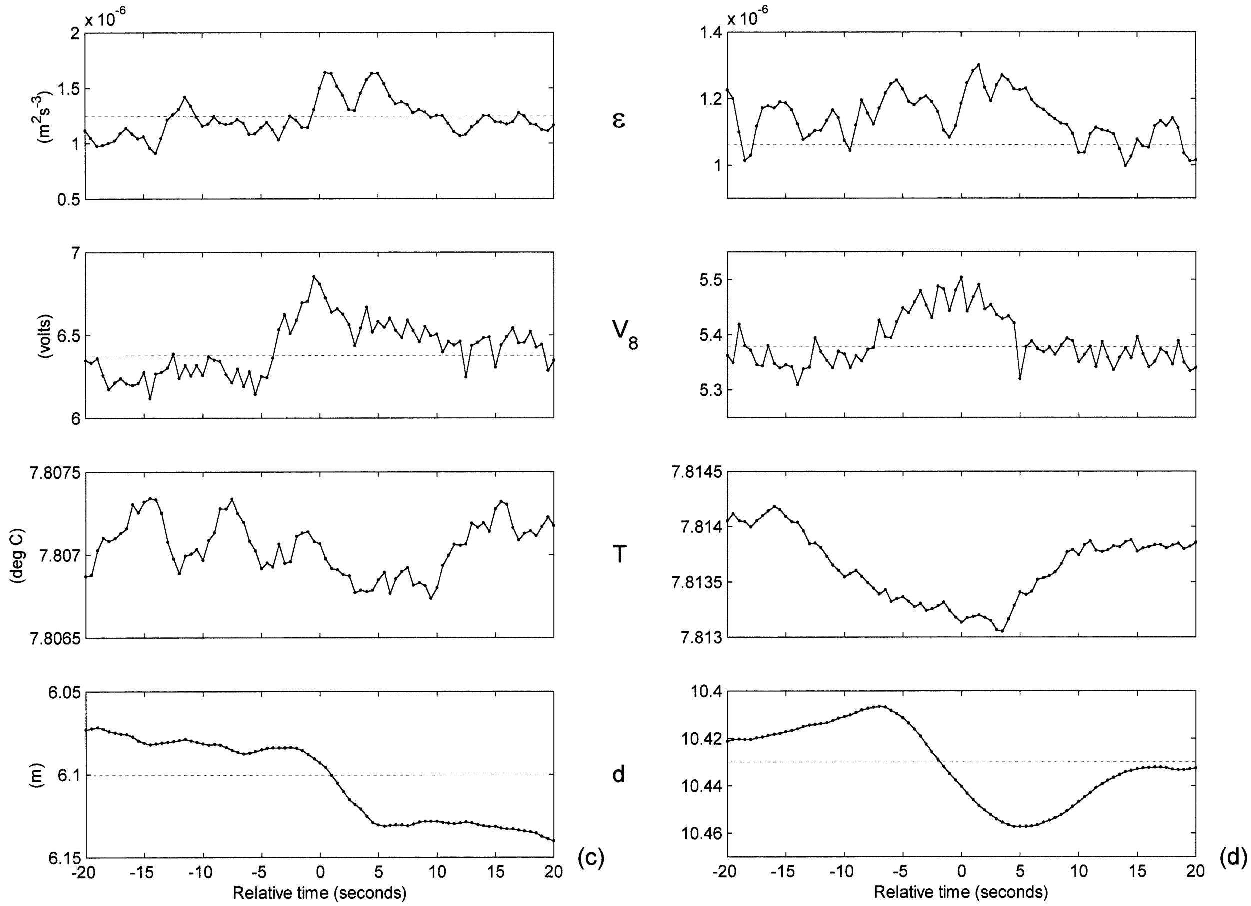


FIG. 8. (*Continued*) the dissipation rate ($\epsilon$), the scattering voltage ($V_8$), temperature ($T$), and depth ($d$). The horizontal dashed lines are mean values. The width of the averaged plots, 40 s, corresponds to an alongtrack distance of 50 m at an angle of 45° to the wind.

only the "stronger" Langmuir cells with faster downward flows will contain bubbles. This provides a means to identify such cells. Figure 9 is a conditional sample plot at an average depth 10.37 m, but only of the bands that contain bubbles at their centers at the depth at which they are traversed by the Autosub. The $\epsilon$, $V_8$, and $T$ signals are enhanced in comparison with those at the same depth in Fig. 8d. The width of the $V_8$ peak is about 8.8 m (10 s), while the $\epsilon$ and $T$ widths are about 17 m; bubbles are confined to a narrower part of the circulation pattern than those within which dissipation rates are enhanced or temperature reduced. The greater vertical displacement, $d$, of the vehicle as it passes through the band, about 0.2 m compared with 0.05 m in Fig. 8d, is consistent with the expected greater downward vertical motions within these bands.

Mean dissipation rates in Langmuir bands exceed $\epsilon_m$ by factors of 1.37, 1.35, 1.49, and 1.71 corresponding to mean mixing lengths, $\Delta z$, of 1.9, 1.2, 1.5, and 1.0 m at $z/H_s$ = 1.92, 4.35, 6.41, and 11.77 in mean wind speeds of 10.6, 11.9, 11.6, and 11.7 m s$^{-1}$, respectively. The corresponding mixing lengths for the circulation cells with bubbles at their centers as they are crossed by Autosub are much greater at depth: 1.9, 1.4, 2.9, and 7.4 m, respectively, indicating their larger vertical transfer, as expected.

### *e. Dissipation rates and acoustic scattering in temperature ramps*

Values of the skewness of the temperature time derivative, $S$, are given in Table 1. The skewness is generally negative in legs directed at acute angles into the wind direction and positive for obtuse angles, consistent with earlier observations during surface cooling when billows or eddies, generated in the wind shear layer, carry colder water downward and strain the temperature field, leading to the formation of temperature ramps (Thorpe et al. 1991).

For convenience, ramps are defined here as locations where

$$[\mathrm{sgn}(S) \times (dT/dt)] \geq [\mathrm{mean}(dT/dt) + 2 \times (\text{the standard deviation of } dT/dt)], \quad (4)$$

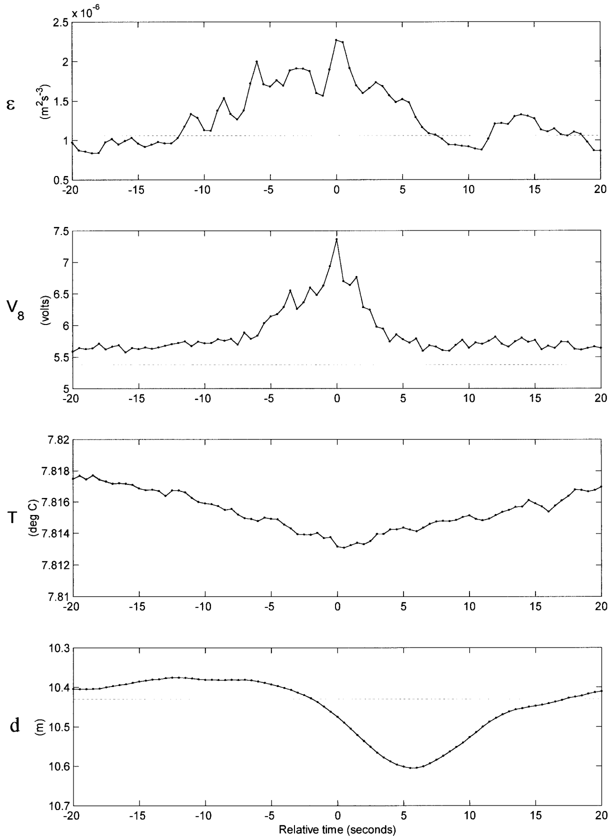


FIG. 9. Conditional sample plot across Langmuir circulation bands with bubble clouds at their centers in a mean wind speed of 11.7 m s$^{-1}$ and a mean depth of 10.43 m. Panels show, top to bottom, the dissipation rate ($\epsilon$), the scattering voltages ($V_8$), temperature ($T$), and Autosub depth ($d$). A total of 33 bands are averaged together. The horizontal dashed lines are mean values. The width of the averaged plots, 40 s, corresponds to an alongtrack distance of 50 m at an angle of 45° to the wind.

where $T$ is the 0.5-s average temperature and $dT/dt$ is found by differencing successive 0.5 s averages. The condition identifies large temperature gradients where $S > 0$, or large negative gradients when $S < 0$. The average distance between ramps is equal to 20.3 m in an average wind speed of 4.7 m s$^{-1}$ (mission 2, legs 12–15, and mission 3) and 22.9 m in relatively steady winds averaging 11.6 m s$^{-1}$ (mission 1: the tracks are at about 45° to the wind for the higher winds, but are in varying relative directions for the lower wind; see Table 1). These distances are similar to the depth of the upper mixing layer and have no significant variation with depth between 2 and 10 m. There is no correlation between the location of temperature ramps and the Langmuir bands.

Figure 10 shows conditional sample plots at times of ramps during legs 1–16 in mission 1 in mean winds of 11.6 m s$^{-1}$. Legs with different values of $S$ have been averaged with time reversed (except for depth that is reversed in sign and with the mean added) so that the sampling direction is effectively at 45° from the wind direction. The cold side of the ramps, indicating water derived from above the sampling level, is associated with enhanced acoustic scatter (as found by Thorpe and Hall 1987) and also with higher $\epsilon$. The width of the regions of acoustic scatter and $\epsilon$ anomalies on either side of the ramp is about 10 m (8 s). [This compares with a distance of about 6.2 m (5 s) in mean winds of 4.7 m s$^{-1}$.] The depth of Autosub changes only slightly at 2 m, but at greater depths decreases on the warm side of ramps and increases in the cold with a mean downward speed of about 1.3 cm s$^{-1}$ at 4 m and 0.8 cm s$^{-1}$ at 6 and 10 m. There is, however, a 2 s difference between the time of zero vertical speed and the time at which the ramps are reached indicating a 2 s or 2.5 m delay in vehicle response. The temperature variance $T_{\rm var}$ (bottom panels) is enhanced in a region of 5 s (about 6.2 m) either side of the ramps.

These variations are consistent with the ramps being associated with shear-induced billows transporting the high bubble content downwards and consequently highly acoustic scattering, and more turbulent, water from the near surface, and replacing it with warmer water with lower $\epsilon$ and fewer bubbles. Using the mean differences between $\epsilon$ on the two sides of the ramps, $\Delta\epsilon$, in (3) gives a mean mixing length of 0.3, 1.3, 2.4, and 1.0 m at $z/H_s = 1.92$, 4.35, 6.41, and 11.77, and mean wind speeds of 10.6, 11.9, 11.6, and 11.7 m s$^{-1}$, respectively, generally comparable to those in Langmuir bands but smaller at depth 2 m. Notable at 10 m (Fig. 10d, top panel) is a narrow peak in $\epsilon$ at the location of the ramp.

## 4. Discussion

### a. The vertical variation of turbulent dissipation rate, $\epsilon$

Dissipation rates follow a law of the wall scaling within the range of steady wind conditions encountered with $1.55 < z/H_s < 15.9$ and $11.7 < c/u_* < 21.7$. This is not inconsistent with Agarwal et al.'s findings of higher dissipations at small depth since the largest values of the depth, $10^5 u_{*w}^2/g$, below which they found the law of the wall to hold is only about 2.4 m (occurring at the highest wind speeds), only slightly in excess of the shallowest mean sampling depths of 2.09 m. Nor does it appear to contradict Terray et al.'s result (2) since the wave age, $c/u_*$, is outside its range of application (see Table 2.).

We may compare the highest values of $\epsilon$, about $5 \times 10^{-5}$ m$^2$ s$^{-3}$, observed at depth 2 m in winds of about 12 m s$^{-1}$ in mission 1 (see Figs. 4a,i) with that which might result directly near the surface from breakers, using the results of Rapp and Melville (1990), Lamarre and Melville (1991), Duncan (1981), and Melville (1994) referred to in section 1. The energy lost per unit time and unit length of a breaker crest is $\chi\rho_w c_b^5/g$, with $\chi = 0.008 \pm 0.004$, and 90% is dissipated within a layer of thickness $H_s$ in a time of 4 periods of the breaking wave ($4T_b$). Suppose that 40% goes into producing bubbles and is not subsequently transmitted into turbulence, and that all the rest is dissipated by turbulence, none going into roller production. Then the mean rate of dissipation of turbulent kinetic energy per unit mass is $0.6 \times 0.9 \times \chi c_b^4/4gH_sT_b$. For dominant waves with $H_s \approx 1$ m of period 4 s, $T_b \approx 2$ s and $c_b \approx 3$ m s$^{-1}$, and the mean dissipation rate in a depth of order 1 m during a period of about 8 s following a breaking event is about $(4.4 \pm 2.2) \times 10^{-3}$ m$^2$ s$^{-3}$, much greater than the highest observed at depth about 2 m and consistent with the assumption that little of the wave-produced turbulence is dissipated at the shallowest depths sampled by Autosub.

The wave number spectra of $\epsilon$ at scales of 5–50 m presumably depend on the distribution of breaking waves and Langmuir cells, but the observed spectral form reported in section 3a remains to be explained.

### *b. Bubble clouds and breakers*

At shallow depths bubble clouds occupy a large fraction of the horizontal area (see section 3b); waves often break in a region of existing bubble clouds and past injection of turbulence by breaking waves. Rarely however are bubble clouds formed by one breaker reinforced by the breaking of a second in the same location within 10–15 wave periods (although one example of such repeated breaking is shown in Fig. 7c.) It appears therefore that turbulence and small scale coherent structures (Thorpe et al. 1999a,b), rollers or residual circulation (Rapp and Melville 1990; Melville et al. 2002) left by breakers do not strongly promote subsequent breaking, but such processes may affect breaking of short capillary–gravity waves, which are not resolved.

Cases shown in Fig. 7 show that breakers do occasionally enhance dissipation rates in the breaker zone to depths of 6 m but that higher dissipation levels there and at 10 m are generally associated with intense and persistent clouds, possibly a consequence of Lc. Dissipation measured after wave breaking at 2.09 m in winds of 11.6 m s$^{-1}$ is consistent with a horizontal spread and downward diffusion or advection of turbulent energy in Lc, reaching depths of about $2H_s$ some 13 wave periods after turbulence is generated, with subsequent decay. This is in fair agreement with Rapp and Melville's (1990) laboratory observations given the variation in the period and height of breakers observed by Gemmrich and Farmer (1999b) (see section 1). The rising values of dissipation rate at greater depths (even to 10.4 m, about $10H_s$ or about 14 times the height of typical breakers found by Gemmrich and Farmer), implies vertical transport rates much greater than found by Rapp and Melville but are in accord with a downward advection at speeds of order 0.1 m s$^{-1}$ by Lc. The turbulence left by breakers is highly variable with typically twice the average standard deviation of $\epsilon$. This may be a consequence of a number of causes—for example, the Autosub's passing through the edge or center of a breaker patch, the variation of turbulence generation in time or space after breaking sets in and the natural variation in breaking depending on whether a wave is spilling or plunging. The energy lost per unit crest length from a breaker depends on the fifth power of its phase speed, $c_b$ (Duncan 1981; Melville 1994), which, like the period of breaking waves (Gemmrich and Farmer 1999b), is subject to considerable variability. Given that a significant fraction is dissipated by turbulence (rather than in bubble production; Lamarre and Melville 1991) this implies a very broad variation in energy loss, consistent with observations.

### *c. Langmuir circulation*

There is a delay of about 2 s between the entry of the temperature and turbulence sensors into a region of downward flow and the response of the pressure sensor on the vehicle (see section 3d; the delay is probably a function of the location of the sensors and the mechanical response of the vehicle). The zero and $-7$ s locations of the zero rate of change of depth at 2 and 10 m in Fig. 8 therefore implies that a downward flow is encountered about 2 and 9 s, respectively, before the vehicle arrives at the center of a bubble band, or accounting for its speed and course, about 1.8 and 8 m, respectively, from the center of the band. It is also noticable that the subsequent variations in $d$ (Fig. 8, fourth panels) increase from about 18 s at depth 2 m to 23 s at 10 m. The average high frequency temperature gradient, $T_{\text{var}}$ (not shown), has no clear pattern of variation across the bands. Two possible explanations sketched in Fig. 11 are that (a) the circulation is distorted and spreads with depth or (b) the bands are tilted. Here AA and BB show the tracks of Autosub at two different depths. The dashed line indicates the position where the vertical velocity of the Lc flow is zero, or approximately where the vehicle's corrected rate of change of depth would be zero. The broadening and general symmetry of the acoustic scattering, dissipation rate, and temperature sections supports this interpretation. It is also in accord with observations of Weller and Price (1988) rather than Fig. 11b. This tilted pattern is drawn to be consistent with the wind direction and the sense of the tilt observed in the temperature field in measurements in Loch Ness (Thorpe and Hall 1982) and interpreted as being a consequence of the Ekman flow (to the left for a wind vector out of the figure) induced by the earth's rotation. That tilt, and consequently rotation, are not important here may be because of the relatively short period of uniform wind forcing.

Some of the features of bubble clouds shown in Fig. 5 are characteristic of those in Lc (Figs. 8, 9). Except for the 2-m depth, the mixing lengths in bubble clouds and within Langmuir bands containing bubble clouds, increase with depth and are of comparable size, sug-

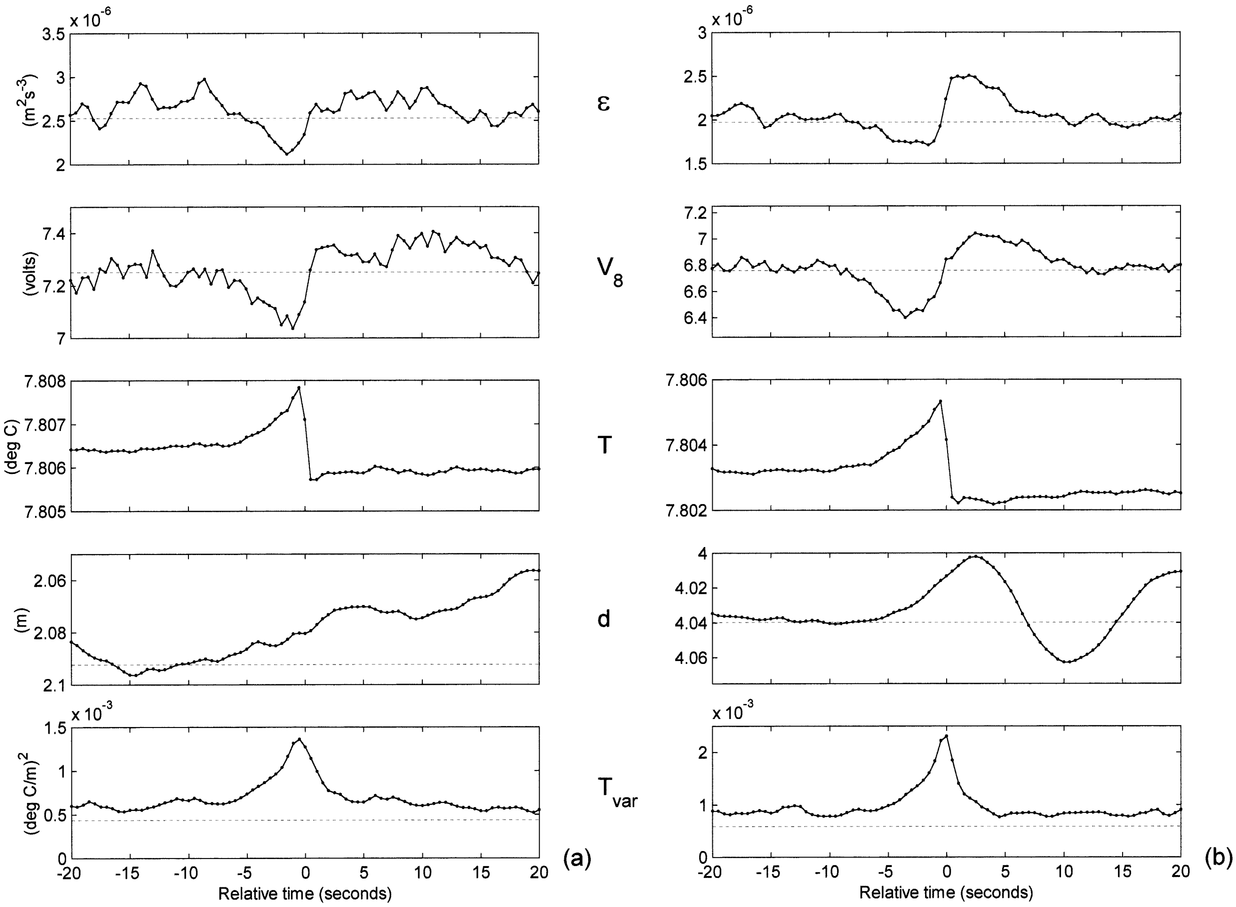


FIG. 10. Conditional sample plot structured about temperature ramps in a mean wind speed of 11.4 m s$^{-1}$ at mean Autosub depths of (a) 2.09 (742 samples), (b) 4.04 (801 samples), (c) 6.10 (363 samples), and (d) 10.43 m (778 samples). The original dataset has been time corrected where necessary so that the ramps are sampled in a direction at about 45° from, but toward, the direction from which the

gesting the deeper bubble clouds are advected by Lc as inferred by Zedel and Farmer (1991) and that such stronger Langmuir cells are important in advecting turbulence generated by breaking waves from the surface to at least 10 m.

The depth of enhanced $\epsilon$ in Lc bands (Figs. 8, 9) is about $12H_s$ or $2.5k^{-1}$, much greater than the Stokes drift scale $(2k)^{-1}$ (approximately equal to 2 m in the corresponding wave conditions) suggested in section 1. The enhancement may be explained as a combination of the advection of turbulent water resulting from waves which break close to the bands (a factor contributing to the bubble cloud concentration in the bands), accompanied by a vertical stretching of turbulent vorticity below the convergence zone and contributions to vertical dispersion from enhanced shear (but see section 4d). Further study is required to establish the relative effect of these processes.

### d. Temperature ramps

It is evident from Fig. 10 that ramps are associated with motions that transport water with relatively high bubble concentration and turbulence downward and warm, low turbulence water with few acoustic scatterers upward, straining the ambient field temperature field to generate temperature microfronts. The enhancement of temperature variance either side of the ramps indicates straining of the field of ambient temperature fluctuations by the shear near the microfront. Figure 12 is a sketch of the ramp structure with the Autosub path drawn in a direction relative to wind consistent with Fig. 10. It shows the associated downward cold flow, enriched with bubbles and with enhanced dissipation encountered after a ramp is crossed. The temperature changes and associated bubbles are consistent with earlier observations (Thorpe and Hall 1980, 1987). No measure of the tilt of the ramp or temperature front is available from the Autosub measurements but earlier measurements find fronts to be inclined at typically 45° to the horizontal. Little is presently known of the cross-wind coherence of temperature ramps.

The average values of dissipation rates within the regions of temperature anomalies surrounding temperature ramps do not differ significantly from the mean

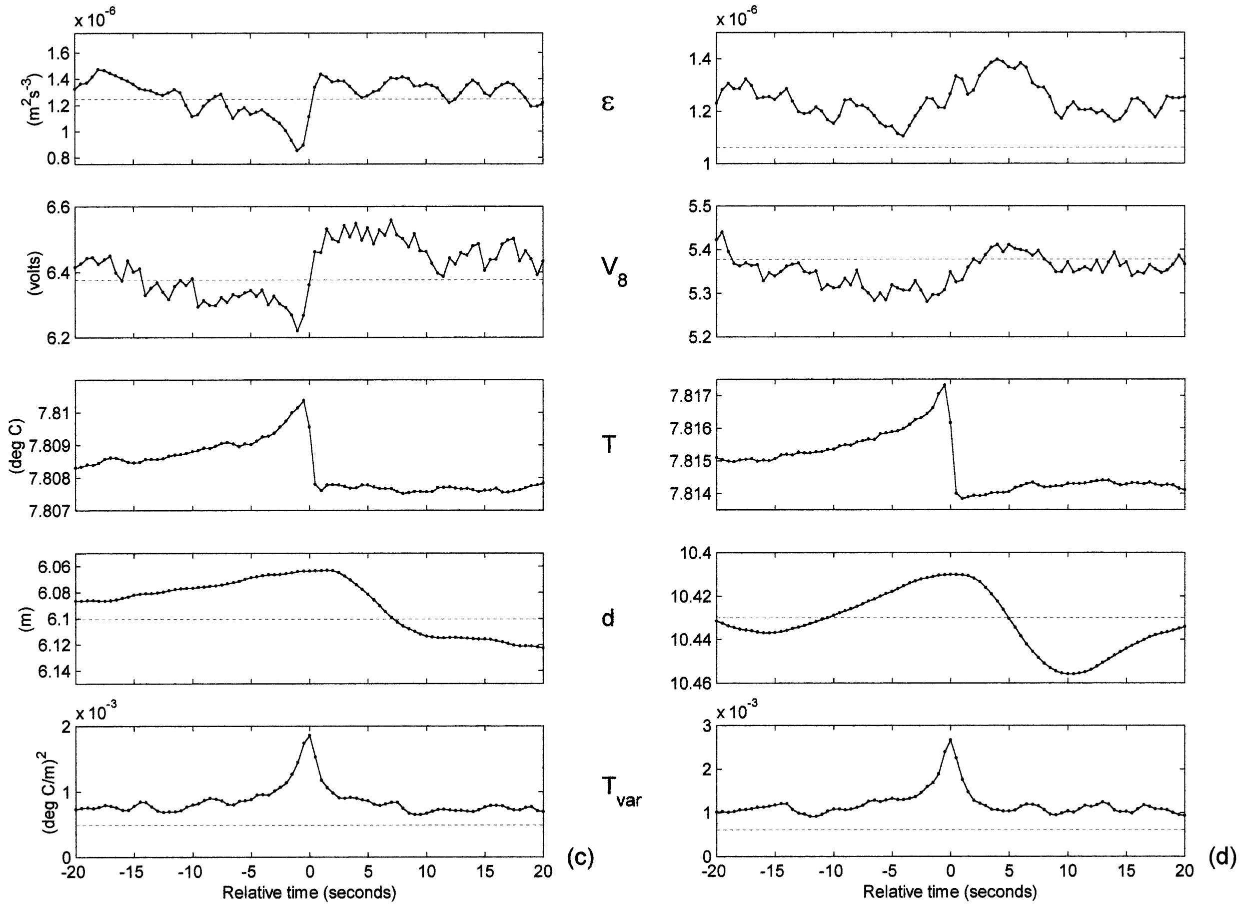


FIG. 10. (*Continued*) wind is coming. The panels show, top to bottom, the dissipation rate ($\epsilon$), the scattering voltage ($V_8$), temperature ($T$), depth ($d$), and temperature variance ($T_{var}$). The horizontal dashed lines are mean values. The width of the averaged plots, 40 s, corresponds to an alongtrack distance of 50 m.

leg-averaged values, $\epsilon_m$. Consequently there is little evidence that the motions that produce the ramps enhance the dissipation rates, although the narrow peak in $\epsilon$ at the location of the ramp at 10 m in Fig. 10d (top panel) suggests that it is a site of weak turbulence generation. The mean mixing lengths in ramps, of order 1 m in winds of 11.4 m s$^{-1}$, is comparable with that in bubble cloud at depth less than about 6 m but less than that generally found in the Langmuir bands at about 2 m and in the bubble-containing Langmuir bands at depths exceeding 5–6 m or about $6H_s$. The mixing lengths in clouds generally, and in Lc in particular, increase with depth, while that associated with ramps decreases below about 6 m, suggesting that while still effective in mixing, they are less so than Lc. This is consistent with the proposal that the motions generating ramps are associated with large eddies occurring near marginal instability of the mean flow (Thorpe and Hall 1977; Thorpe 1978), a means of relaxing the shear and stirring the density field without being major generators of turbulence, unlike the smaller-scale turbulent eddies that derive substantial energy from the shear flow.

## 5. Conclusions

The direct measurements of $\epsilon$ in the mixed layer where $z > 1.55H_s$ show its relation to breaking waves, Lc, and temperature ramps. There is a strong ''input'' association between bubble clouds and turbulent dissipation, as both bubbles and turbulence are generated within breaking waves. Within about one wave period from the onset of breaking, turbulence fragments the larger bubbles (Garrett et al. 2000), their rising contributes to the turbulent motion, and, reaching the surface, the bubbles burst or contribute to foam (Farmer et al. 1999; Thorpe et al. 1999a,b). The slowly rising, small (~100 $\mu$m radii) bubbles left beneath the surface subsequently provide a useful, but not exact, tracer of small-scale turbulence generated by the breakers over short periods of time when advection is rapid. The connection must ultimately fail because the two respond to different processes. Although the small-scale turbulence is advected, it decays unless locally enhanced by, for example, a local strain field, while bubbles are subject to changes in radius caused by dissolution, surface ten-

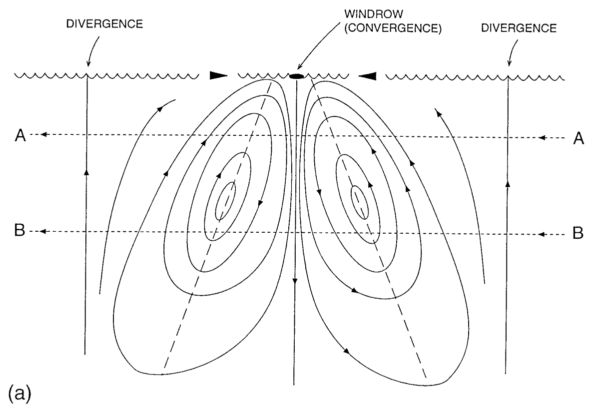


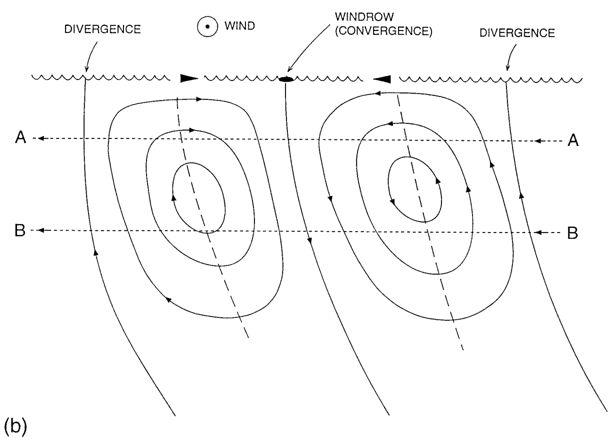


FIG. 11. Sketch of conceptual circulations within Langmuir circulation bubble bands. The model (a) is of a pattern symmetric about the vertical plane through the windrow with the centers of the streamline pattern relatively near the windrow location. The dashed lines mark positions where the streamlines and the flow are horizontal. Here AA and BB show two Autosub tracks. Downward flow is encountered where the vehicle crosses the dashed lines, farther from the center of the pattern at greater depth, BB. In model (b) the wind direction is out of the paper and the circulation is tilted by the effect of the Ekman spiral flow. The locations of horizontal flow are again marked by dashed lines and are encountered earlier in the deeper track BB.

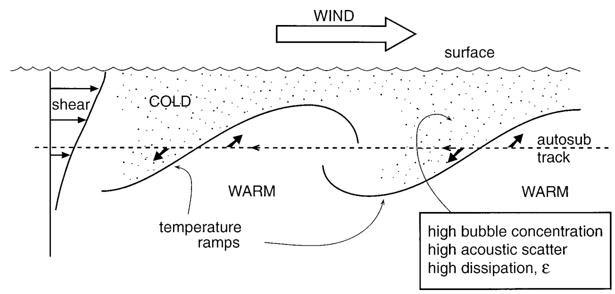


FIG. 12. Sketch of the structure in a temperature ramp showing the downward-moving colder bubble-enriched water with higher dissipation on one side and the warmer rising water on the other. The dashed line shows the track of Autosub passing through ramps in an upwind direction as in Fig. 10.

sion, and pressure forces, and buoyancy forces cause their rise through the surrounding, advecting fluid. The observed *association* of turbulent dissipation and bubbles within bubble clouds and in the two major processes, Lc and shear instability leading to temperature ramps, does not in itself prove that both bubbles and small-scale turbulence are strongly advected from their joint source in breakers by the motion fields of the processes, but is a strong indication that this is so.

It appears remarkable that, even in the presence of Lc, mean turbulent dissipation rates still conform to (1), scaling as for a rigid boundary. This suggests that Lc, believed to result as a consequence of Stokes drift in the local wave field (Leibovich 1983) and significant in advecting turbulence (Figs. 8,9; section 3d), scales with $u_{*w}$, and that the waves and the circulation introduce no significant new length or velocity scales affecting the turbulence beyond a depth of about $1.2H_s$. It is a demonstration that the law of the wall is independent of the nature of physical processes transferring momentum provided that their magnitude and effect are determined, or scaled, only by the boundary stress (or $u_{*w}$) and distance, $z$. D'Asaro (2001) finds that the rms vertical velocity in the mixed layer scales with $u_{*w}$ but with a coefficient of proportionality 1.75–2.0 greater than that for a rigid wall, perhaps explained by the effect of Lc. Smith (1999) however finds that surface velocities in Lc scale with the Stokes drift (although the coefficient of proportionality depends on some other, yet unspecified, parameter). The precise scaling of motion in Lc is not known and further research is required. The wave age or swell generated by a distant storm offer additional parameters or scales that might effect Lc scaling.

Much of what has been found confirms what was known earlier about the relations between bubble clouds, temperature variations, and Lc, but the results add important quantitative measures of dissipation and, in particular, identify the importance of Lc as a process leading to locally enhanced regions of turbulent dissipation that dominates others (e.g., temperature ramps) at depths exceeding about $6H_s$. The finding that the high rates of turbulent dissipation near the surface occur predominantly in bubble clouds may have biological and chemical consequences, for example, in the generation of foams and scums or in air–sea gas transfer. The results described here allow the assumptions generally made in modeling bubble clouds and air–sea gas transfer via bubbles (e.g., see Thorpe 1986a) to be tested, and this will be addressed elsewhere. It is evident that further measurements are required in a broader range of sea states and especially at depths less than one significant wave height. This will be possible using Autosub in longer and higher waves.

*Acknowledgments.* We are grateful to the assistance and support of the Autosub team led by Nick Millard and to the master and crew of the *Tershelling*, without whose support the measurements reported above could not have been made. Facilities and, for the preliminary trials, the use of the R/V *Calanus*, were kindly provided by the Director of the Marine Biological Laboratory at Dunstaffnage. The study was supported by the UK NERC AUTOSUB Special Topic Science Programme under Grant GST/02/2157 and by the U.S. ONR. In addition to the sensors described above, Autosub carried a bubble resonator kindly loaned by Dr. David Farmer. The results obtained from that instruments will be the subject of a subsequent paper.

## APPENDIX

### Autosub

The self-propelled AUV, Autosub, is operated by the Southampton Oceanography Centre and is 7 m long with a circular section of diameter 0.9 m. It is consequently comparable in size to the U.S. Navy's Large Diameter Unmanned Underwater Vehicle and much larger than the AUV designed by the Florida Atlantic University, previously used for upper ocean turbulence measurement by Levine and Lueck (1999) and Dhanak and Holoppa (1999), respectively. Autosub collected GPS fixes while at the surface, typically before its first dive and subsequently at about 4-h intervals, navigating between preset way points by dead reckoning. As standard equipment, it carries a CTD and 300-kHz broadband ADCP. Its collision-avoidance sonar was switched off after the first mission when it was found that while at 6-m depth in wind speeds of 12.2 m $s^{-1}$, the sonar had initiated avoidance action after incorrectly recognizing intense bubble clouds as solid targets. While improvements to performance have since been made, at the time of the experiments in March–April 2000, it was capable of undertaking unattended missions lasting for 48 h to depths of 300 m and operated at speeds through the water of about 1.25 m $s^{-1}$ when equipped with our instruments.

#### *a. The turbulence package*

A turbulence package was mounted on a firm, but vibration-damping support on the nose of the Autosub. Instrumentation for measuring the dissipation rates $\epsilon$, temperature $T$, and temperature gradient variance $T_{var}$ is much the same as described by Osborn et al. (1992). The package, a 0.14-m-diameter, 0.8-m-long pressure tube, supports two airfoil probes for velocity microstructure (Osborn and Crawford 1980; Osborn and Lueck 1985), a FP07 thermistor for temperature and its gradient, a pressure transducer, and three orthogonal accelerometers. The package extends 0.7 m ahead of the vehicle nose, with probes 0.15 m farther forward. A protective sheath covers and protects the probes from floating objects when Autosub is on the surface and retracts on diving. Values for dissipation rates are normally estimated every 1.0 s, corresponding to horizontal distances of about 1.25 m.

The recording system of the turbulence package is based on a PC104 style AMPRO 386 embedded computer using a DR-DOS operating system, a Real Time devices 16 channel, 16 bit A/D card (DM 5416), an ethernet card and two 8 megabyte hard disks. The system records duplicate copies of the data by digitizing all channels at 512 Hz and writing to buffers in memory that are transferred to disk every 6 s. The two airfoil probes are connected to high impedance amplifiers after which the signal is differentiated electronically. Signals are filtered to prevent aliasing. Pressure measurements are made with a Viatran (300 psi full scale) strain-gauge transducer. Circuitry is unusual; the output is a combination of both pressure and its time derivative. This combination allows use of the technique of Mudge and Lueck (1994) to reconstruct a high-resolution pressure record (Osborn et al. 1992). The two signals are combined and digitized so that the frequency response is flat to above 1 Hz. Laboratory calibrations of the transducer give the sensitivity to a few percent, although offset must be determined before launch. The offset drifts over time and so mean vehicle depth is derived from the Autosub CTD whilst variations are from the turbulence package.

The temperature sensor (Thermometric FP07) is connected to a Wheatstone bridge and then amplified and differentiated. As with pressure, the digitized signal contains both temperature and its derivative up to frequencies of 55 Hz, which exceeds thermistor response frequency, a technique used previously by Osborn (1991). The three Sundestrand QC-1300 accelerometers are mounted in the nose of the turbulence package. They are aligned to sense axial, lateral, and vertical accelerations relative to the package. The measured signals are pitch, roll, and heave in addition to structural vibrations. The circuits and sensors have been in use for over 20 years.

Dissipation rates are calculated in two different ways. The first is designed to provide spatial resolution of 1 s for the dissipation data to compare with the sonar data. In this case, signal to noise is lower to get better spatial resolution. The second is to get leg-average dissipations with a better signal to noise ratio. Any difference in the mean values of the two calculations is due to vibrations associated with mounting the turbulence package on Autosub.

Accelerometer spectra show a broad band of vibration between 10 and 20 Hz. With a strong signal (e.g., in mission 1 and at the end of mission 4) these vibrations do not affect the dissipation calculations. However, when the shear signal is lower (e.g., missions 2 and 3), they contribute to the variance of the measured shear spectrum. There are also narrow vibration peaks, most notably near 70 Hz. The dissipation rates with 1-s resolution are integrals of the shear spectrum to 40 Hz in low dissipation regimes and 140 Hz in high. Narrow vibration peaks are deleted and replaced with average values from adjacent frequencies. The dissipations are corrected for the fraction above the upper limit of integration using the ''Nasmyth universal shape'' reported by Oakey (1982).

The technique of Levine and Lueck (1999) is used to calculate average dissipation along each leg. The fraction that is coherent with the appropriate accelerometer is subtracted from the variance of the shear signal. Four minute intervals of data are spectrally analyzed as overlapping two second segments to calculate the power and cross-spectra of the shear and accelerometer signals. Dissipation rates are again integrated to 40 and 140 Hz with the Nasmyth universal shape to correct for the limited range of integration. The average dissipation rates along each leg of mission 1 using these calculations and those from 1-s values agree to 5%. With the lower mean dissipation rates of mission 2 the averages of 1-s values ate 10% to 80% higher as a result of variance contribution from mounting vibration. Dissipation rates less than $5 \times 10^{-9}$ m$^2$ s$^{-3}$ are observed in mission 2 and probably represent the noise floor for the 1-s averages.

Uncertainty in dissipation rate estimates arises in probe calibration, variations in axial speed, and angle of attack due to wave orbital motions and variations in vehicle speed. Flow distortion caused by the proximity of Autosub and the turbulence package and its effect was calculated using potential flow theory for elliptical shapes (Lamb 1945). There is a 7% reduction in speed and a concomitant compression of axial wavelengths and these were accounted for in the dissipation calculations. Autosub has low drag and the axial response to wave orbital motion is low. The spatial spectra of dissipations at depth 2 m in the stronger wind conditions show a peak at surface wave frequencies. Dissipation rates are proportional to the fourth power of the axial speed and assuming too low (or high) an axial speed makes calculated dissipations too high (or low, respectively). The nonlinear effect is likely to skew dissipation rates to higher, rather than lower, values. At the operational depths (see Table 1), the effect of bubble clouds on estimates of $\epsilon$ is negligible (see Osborn et al. 1992). Previous values of overall uncertainty in dissipation have been about 50%. Estimates are that the uncertainty in individual values is larger here by a factor of about 2, largely as a consequence of the effects of waves. For leg average values, $\epsilon_m$, the uncertainty is about 50%, and it is less than 10% for ratios of mean values used in estimating mixing lengths.

### *b. Sidescan sonars*

Autosub also carried a sonar package, ARIES II (Thorpe et al. 1998), with two 250-kHz sidescan sonar transducers operating with pulse repetition rates of 2 Hz, the same as those used previously in studies of bubble clouds (Thorpe and Hall 1983). Each transducer has a beam angle of 33° wide in the vertical and 1.6° in the horizontal, beam angles being measured to the −3 dB points. One sonar is mounted on top of Autosub, 1.49 m behind the turbulence sensors, tilted up at 28° from the horizontal and pointed forward to detect breaking waves and bubble clouds ahead of the AUV. The other, 0.25 m behind the first, is pointed to the starboard and tilted up at 25° to detect nearby bubble clouds and bubble bands produced by Lc.

### *c. Trials*

Preliminary trials were made in Loch Linnhe, in northwest Scotland in April 1999 and in March 2000 before the main science missions, to develop deployment and recovery strategies, and to examine possible untoward interference between the Autosub, sonars, and turbulence package sensing and recording systems.

## REFERENCES


Agarwal, Y. C., E. A. Terray, M. A. Donelan, P. A. Hwang, A. J. Williams III, W. M. Drennan, K. K. Kahma, and S. A. Kitagorodskii, 1992: Enhanced dissipation of kinetic energy beneath surface waves. *Nature,* **359,** 219–220.

Anis, A., and J. N. Moum, 1995: Surface wave-turbulence interactions. Scaling $\epsilon(z)$ near the sea surface. *J. Phys. Oceanogr.,* **25,** 2025–2045.

Antonia, R. A., A. J. Chambers, C. A. Friehe, and C. W. Van Atta, 1979: Temperature ramps in the atospheric boundary layer. *J. Atmos. Sci.,* **36,** 99–108.

Brown, G., and A. Roshko, 1974: On density effects and large structure in turbulent mixing layers. *J. Fluid Mech.,* **64,** 775–816.

Craig, P. D., and M. L. Banner, 1994: Modeling wave-enhanced turbulence in the ocean surface layer. *J. Phys. Oceanogr.,* **24,** 2546–2559.

Csanady, G. T., 1994: Vortex pair model of Langmuir circulation. *J. Mar. Res.,* **52,** 559–581.

——, 2001: *Air–Sea Interaction.* Cambridge University Press, 239 pp.

D'Asaro, E. A., 2001: Turbulent vertical kinetic energy in the ocean mixed layer. *J. Phys. Oceanogr.,* **31,** 3530–3537.

Dhanek, M. R., and K. Holappa, 1999: An autonomous ocean turbulence measurement platform. *J. Atmos. Oceanic Technol.,* **16,** 1506–1518.

Drennan, W. M., M. A. Donelan, E. A. Terray, and K. B. Katsaros, 1996: Oceanic turbulence dissipation measurements in SWADE. *J. Phys. Oceanogr.,* **26,** 808–814.

Duncan, J. H., 1981: An investigation of breaking waves produced by a towed hydrofoil. *Proc. Roy. Soc. London,* **377A,** 331–348.

Farmer, D. M., and M. Li, 1995: Patterns of bubble clouds organized by Langmuir circulation. *J. Phys. Oceanogr.,* **25,** 1426–1440.

——, and J. R. Gemmrich, 1996: Measurements of temperature fluctuations in breaking surface waves. *J. Phys. Oceanogr.,* **26,** 816–825.

——, C. McNeil, and B. Johnson, 1993: Evidence for the importance of bubbles to the enhancement of air–sea gas flux. *Nature,* **361,** 620–623.

——, S. Vagle, and M. Li, 1999: Wave breaking, turbulence and bubble distributions in the ocean surface layer. *The Wind-Driven Air–Sea Interface*, M. Banner, Ed., School of Mathematics, The University of New South Wales, Sydney, Australia, 187–192.

Garrett, C., M. Li, and D. Farmer, 2000: The connection between bubble size spectra and energy dissipation rates in the upper ocean. *J. Phys. Oceanogr.,* **30,** 2163–2171.

Geernaert, G. L., 1990: Bulk parametrizations for the wind speed and heat fluxes. *Surface Waves and Fluxes,* G. L. Geernaert and W. J. Plant, Eds., Vol. 1, Kluwer Academic, 91–172.

Gemmrich, J. R., 2000: Temperature anomalies beneath breaking waves and the decay of wave-induced turbulence. *J. Geophys. Res.,* **105,** 8727–8736.

——, and D. M. Farmer, 1999a: Near surface turbulence and thermal structure in a wind driven sea. *J. Phys. Oceanogr.,* **29,** 480–499.

——, and ——, 1999b: Observations of the scale and occurrence of breaking surface waves. *J. Phys. Oceanogr.,* **29,** 2595–2606.

Gerz, T., and U. Schumann, 1996: A possible explanation of countergradient fluxes in homogeneous turbulence. *Theor. Comput. Fluid Dyn.,* **8,** 169–181.

——, J. Howell, and L. Mahrt, 1994: Vortex structures and microfronts. *Phys. Fluids.,* **6,** 1242–1251.

Jessup, A. T., C. J. Zappa, and H. Yeh, 1997: Defining and quantifying microscale wave breaking with infrared imagery. *J. Geophys. Res.,* **102,** 23 145–23 153.

Keller, K. H., and C. W. Van Atta, 2000: An experimental investigation of the vertical temperature structure of homogeneous stratified shear turbulence. *J. Fluid Mech.,* **425,** 1–29.

Lamarre, E., and W. K. Melville, 1991: Air entrainment and dissipation in breaking waves. *Nature,* **351,** 469–472.

Lamb, H., 1945: *Hydrodynamics.* 6th ed. Cambridge University Press, 738 pp.

Leibovich, S., 1983: The form and dynamics of Langmuir circulations. *Ann. Rev. Fluid Mech.,* **15,** 391–427.

——, and A. Tandon, 1993: Three-dimensional Langmuir circulation instability in a stratified layer. *J. Geophys. Res.,* **98,** 16 501–16 507.

Levine, E. R., and R. G. Lueck, 1999: Turbulence measurements from an autonomous underwater vehicle. *J. Atmos. Oceanic Technol.,* **16,** 1533–1544.

Li, M., and C. Garrett, 1993: Cell merging and the jet/downwelling ratio in Langmuir circulation. *J. Mar. Res.,* **51,** 737–769.

Massel, S. R., 1996: Ocean surface waves: their physics and prediction. *Advanced Series on Ocean Engineering,* Vol. 11., World Scientific, 231 pp.

McLeish, W., 1970: Spatial spectra of ocean surface temperature. *J. Geophys. Res.,* **75,** 6872–6877.

McWilliams, J. C., P. P. Sullivan, and C.-H. Moeng, 1997: Langmuir turbulence in the ocean. *J. Fluid Mech.,* **334,** 1–30.

Melville, W. K., 1994: Energy dissipation by breaking waves. *J. Phys. Oceanogr.,* **24,** 2041–2049.

——, 1996: The role of surface-wave breaking in air–sea interaction. *Ann. Rev. Fluid Mech.,* **28,** 279–321.

——, F. Veron, and C. J. White, 2002: The velocity field under breaking waves: Coherent structures and turbulence. *J. Fluid Mech.,* **454,** 203–234.

Millard, N. W., and Coauthors, 1998: Versatile autonomous submersibles—The realisation and testing of a practical vehicle. *Underwater Technol.,* **23,** 7–17.

Mitsuyasu, H., 1985: A note on momentum transfer from wind to waves. *J. Geophys. Res.,* **90,** 3343–3345.

Mudge, T. D., and R. G. Lueck, 1994: Digital signal processing to enhance oceanographic observations. *J. Atmos. Oceanic. Technol.,* **11,** 825–836.

Oakey, N., 1982: Determination of the rate of dissipation of turbulent energy from simultaneous temperature and velocity shear measurements. *J. Phys. Oceanogr.,* **12,** 256–271.

Osborn, T., 1991: Observations of the ''Salt Fountain''? *Atmos.–Ocean,* **29,** 340–351.

——, and W. R. Crawford, 1980: An airfoil probe for measuring turbulent velocity fluctuations in water. *Air–Sea Interaction: Instruments and Methods,* F. Dobson et al., Eds., Plenum, 801 pp.

——, and R. G. Lueck, 1985: Turbulence measurements from a submarine. *J. Phys. Oceanogr.,* **15,** 1502–1520.

——, D. M. Farmer, S. Vagle, S. A. Thorpe, and M. Cure, 1992: Measurements of bubble plumes and turbulence from a submarine. *Atmos.–Ocean,* **30,** 419–440.

Rapp, R. J., and W. K. Melville, 1990: Laboratory measurements of deep-water breaking waves. *Philos. Trans. Roy. Soc. London,* **331A,** 735–800.

Shay, T. T., and M. C. Gregg, 1986: Convectively driven turbulent mixing in the upper ocean. *J. Phys. Oceanogr.,* **16,** 1777–1798.

Skyllingstad, E. D., and D. W. Danbo, 1995: An ocean large-eddy simulation of Langmuir circulations and convection in the surface layer. *J. Geophys. Res.,* **100,** 8501–8522.

Smith, J. A., 1999: Observations of wind, waves and the mixed layer: The scaling of surface motions. *The Wind-Driven Air–Sea Interface,* M. L. Banner, Ed., School of Mathematics, The University of N. S. Wales, Sydney, Australia, 231–238.

Terray, E. A., M. A. Donelan, Y. C. Agarwal, W. M. Drennan, K. K. Kahma, A. J. Williams III, P. A. Hwang, and S. A. Kitagorodshii, 1996: Estimates of kinetic energy dissipation under breaking waves. *J. Phys. Oceanogr.,* **26,** 792–807.

Thorpe, S. A., 1978: The near-surface ocean mixing layer in stable heating conditions. *J. Geophys. Res.,* **83,** 2875–2885.

——, 1982: On the clouds of bubbles formed by breaking wind-waves in deep water, and their role in air–sea gas transfer. *Philos. Trans. Roy. Soc. London,* **304A,** 155–210.

——, 1984: The effects of Langmuir circulation on the distribution of submerged bubbles caused by breaking wind waves. *J. Fluid Mech.,* **114,** 237–250.

——, 1985: Small-scale processes in the upper ocean boundary layer. *Nature,* **318,** 519–522.

——, 1986a: Bubble clouds: A review of their detection by sonar, of related models, and how Kv may be determined. *Oceanic Whitecaps,* E. C. Monahan and G. MacNiocaill, Eds., D. Reidel, 57–68.

——, 1986b: Measurements with an automatically recording inverted echo sounder, ARIES and the bubble clouds. *J. Phys. Oceanogr.,* **16,** 1462–1478.

——, 1992a: The break-up of Langmuir circulation and the instability of an array or vortices. *J. Phys. Oceanogr.,* **22,** 350–360.

——, 1992b: Bubble clouds and the dynamics of the upper ocean. *Quart. J. Roy. Meteor. Soc.,* **118,** 1–22.

——, 1995: Dynamical processes of transfer at the sea surface. *Progress in Oceanography,* Vol. 35, Pergamon, 315–352.

——, and A. J. Hall, 1977: Mixing in upper layer of a lake during heating cycle. *Nature,* **265,** 719–722.

——, and ——, 1980: The mixing layer of Loch Ness. *J. Fluid Mech.,* **101,** 687–703.

——, and ——, 1982: Observations of the thermal structure of Langmuir circulation. *J. Fluid Mech.,* **114,** 237–250.

——, and ——, 1983: The characteristics of breaking waves, bubble clouds, and near-surface currents observed using side-scan sonar. *Cont. Shelf Res.,* **1,** 353–384.

——, and ——, 1987: Bubble clouds and temperature anomalies in the upper ocean. *Nature,* **328,** 48–51.

——, M. Cure, and M. White, 1991: The skewness of temperature derivatives in oceanic boundary layers. *J. Phys. Oceanogr.,* **21,** 428–433.

——, M. J. Ulloa, D. Baldwin, and A. J. Hall, 1998: An Autonomously Recording Inverted Echo Sounder: ARIES II. *J. Atmos. Oceanic Technol.,* **15,** 1346–1360.

——, W. Nimmo Smith, A. Graham, and A. Thurnherr, 1999a: Patterns in foam and shallow tidal flows. *The Wind-Driven Air–Sea Interface,* M. Banner, Ed., School of Mathematics, The University of New South Wales, Sydney, Australia, 257–264.

——, ——, A. Thurnherr, and N. J. Walters, 1999b: Patterns in foam. *Weather,* **54,** 327–334.

Weller, R. A., and J. F. Price, 1988: Langmuir circulation within the oceanic mixed layer. *Deep-Sea Res.,* **35,** 711–747.

Zedel, L., and D. M. Farmer, 1991: Organised structures in subsurface bubble clouds: Langmuir circulation in the open ocean. *J. Geophys. Res.,* **96,** 8889–8900.